Morphological Segmentation for Textures and Particles

Luc Vincent
Xerox Imaging Systems, Peabody MA

Edward R. Dougherty
Center for Imaging Science, Rochester Institute of Technology

Published as Chapter 2 of *Digital Image Processing Methods,* E. Dougherty, Editor, Marcel-Dekker, New York, 1994, Pages 43--102.

1 Introduction, Morphological Segmentation

The present chapter concerns image segmentation via the methods of morphological image processing. A generally accepted meaning of the word *segmentation* in the image processing community is the decomposition of the image under study into its different areas of interest. Here, we shall take the perspective that there are essentially two kinds of segmentation: segmentation of images of *texture* and segmentation of images of *particles.*

In texture segmentation, an image is partitioned into regions, each of which is defined by some set of features characteristic to the micro image structure within it, this structure typically being viewed in terms of the small *texture primitives* composing it. Typical applications include segmentation of vegetation types in aerial photographs, segmentation of text and halftones in document pages, and medical imaging applications (like the extraction of bone tissue according to trabecular structure in magnetic resonance images [15], see Fig. 10).

The second kind of segmentation is concerned with images of particles (or objects), where textural information is either not present, or cannot be simply used as a discriminating factor. The segmentation task consists of extracting the particles from the image(s) under study. In other words, the goal is to partition the image in as many connected components as there are objects or regions to extract, plus some background regions. We distinguish between binary and grayscale particle segmentation: in the binary case, i.e. when the images under study are binary, the segmentation task consists in separating the overlapping particles (e.g., see the coffee beans example of Fig. 11a). In the grayscale case, the segmentation task is equivalent to a contour extraction problem (e.g., in Fig. 11b, the contours of the electrophoresis spots have to be extracted as precisely as possible).

The chapter is divided into two sections, the first concerning regional texture oriented segmentation and the second concerning particle segmentation. The literature on image processing of textures is too abundant to be thoroughly reviewed in this chapter, even if we restricted ourselves to purely morphological methods. Instead, we focus on the approach based on *local granulometries,* which offers an intuitive formulation, can be applied to a wide range of images, and can be used for both texture segmentation and classification. In this section, we only deal with binary images, but the method can be used for graycale images equally well (see example of Fig. 10) As concerns particle segmentation, we shall mainly concentrate on *watershed* segmentation, which has the advantages of being very general, usually accurate and fast, and applicable to both binary and grayscale images.

Both segmentation paradigms involve a fair amount of morphological machinery and, subject to the space constraint of a single chapter, we shall introduce the necessary machinery, leaving detailed theoretical descriptions to the literature. We refer to Chapter X of this book for the definitions and properties of the basic morphological operations, together with the notations used to represent them, and to [22] for an introductory account of the fundamentals of morphological image processing. For a more advanced coverage of mathematical morphology, one can consult the books by Serra [45, 46] and the review paper [47].

2 Granulometric Segmentation of Textures

2.1 Granulometries Generated by a Single Structuring Element

As originally conceived for binary images [34], granulometries are employed to characterize size and shape information within granular binary images via the manner in which they are sieved through various sized and shaped sieves. If an image is considered as a collection of grains, then whether or not an individual grain will pass through a sieve depends upon its size and shape relative to the mesh of the sieve. By increasing mesh size, ever more grains within the image will pass through, the eventual result being that no grains will remain. Of course, this sieving model does not fully describe even a granular image, for in a real image the grains will likely overlap; nevertheless, it does serve as a means to approach the removal of nonconforming image structure and can be further developed to obtain image signatures based on the rate of sieving.

We begin by considering the most basic type of granulometry for Euclidean images, which by definition are considered to be closed subsets of the Euclidean plane. A fundamental result of mathematical morphology [34] states that a compact set B is convex if and only if, whenever $r > s > 0$, rB is sB-open, the latter meaning that $rB \circ sB = rB$ (Recall that $rB = \{rb \mid b \in B\}$ is the homothetic or scalar multiple of the set B by the real number r and that $\circ$ denotes the morphological opening.). A basic property of opening is that if E is B-open, then, for any set A, $A \circ E$ is a subset of $A \circ B$. Thus, if B is convex, $r > s > 0$ implies $A \circ rB$ is a subset of $A \circ sB$. If we think of grains in the image A falling through the holes sB and rB, more will fall through the hole rB, thereby yielding a more diminished filtered image. Indeed, since rB is sB-open, it can be shown not only that $A \circ rB$ is a subset of $A \circ sB$ but also that

$$(A \circ rB) \circ sB = (A \circ sB) \circ rB = A \circ rB, \tag{1}$$

so that iteratively opening, in either order, is equivalent to opening only by rB.

Definition 1 (Granulometry) *If we consider $t > 0$ as a variable, then the family $\{A \circ tB\}$ of opened images, B convex, is called a granulometry.*

(Note: we shall give in section 2.4 a more general definition of granulometries.) If $\Omega(t)$ is the area of $A \circ tB$, with $\Omega(0)$ being the area of A itself, then $\Omega(t)$ is a decreasing function of t, known as a *size distribution.* Under the assumption that A is bounded, $\Omega(t) = 0$ for sufficiently large t.

One can now define the *normalized size distribution* as $\Phi(t) = 1 - \Omega(t)/\Omega(0)$. It can be shown that $\Phi(t)$ increases from 0 to 1 and is continuous from the left [34], and we can therefore propose the following definition:

Definition 2 (Normalized size distribution) *The normalized size distribution*

$$\Phi(t) = 1 - \frac{\Omega(t)}{\Omega(0)} \tag{2}$$

is a probability distribution function known as the granulometric size distribution of A with respect to the generator B.

As a result, the derivative of $\Phi(t)$, $\Phi'(t) = d\Phi(t)/dt$ is a probability density, that is sometimes also called the granulometric size distribution, or, of more recent vintage, the *pattern spectrum* of the image A relative to the *generator* B. Since $\Phi'(t)$ is a probability density, it possesses moments. These are employed as image signatures.

To practically apply the granulometric method we first have to adapt it to digital images, which in the present section are assumed to be subsets of the square Cartesian grid $\mathbb{Z}^2$. This cannot be done directly owing to two difficulties regarding the Cartesian grid: first, the lack of an appropriate notion of convexity; second, the inability to apply scalar multipication by arbitrary real numbers. The method of granulometric generation we now discuss is applicable to both Euclidean images and discrete images, its main purpose being application to the latter.

Consider a sequence $E_1, E_2, \ldots$ of structuring elements of increasing size, where E_{k+1} is E_k-open for all k. Owing to the latter requirement, if S is any image, then $S \circ E_{k+1}$ is a subimage of $S \circ E_k$. Consequently, opening in turn by the structuring elements yields a decreasing sequence of images:

$$S \circ E_1 \supseteq S \circ E_2 \supseteq S \circ E_3 \supseteq \ldots \tag{3}$$

For each k, let $\Omega(k)$ be the number of pixels in $S \circ E_k$. Then $\Omega(k)$ is a decreasing function of k. Under the assumptions that E_1 consists of a single pixel and that S is finite, $\Omega(1)$ gives the original pixel count in S and $\Omega(k) = 0$ for sufficiently large k. Applying the normalization of Eq. (2) with k in place of t and 1 in place of 0 yields a normalized size distribution $\Phi(k)$. It is a discrete probability distribution function and possesses a discrete derivative

$$\Phi'(k) = d\Phi(k) = \Phi(k+1) - \Phi(k) \tag{4}$$

which is a discrete density (probability mass function). Again, the density is called a granulometric size distribution or pattern spectrum, and its moments can be employed as image signatures.

There exists a straightforward approach to forming sequences $\{E_k\}$ such that E_{k+1} is E_k-open: choose a primitive E and let E_1 be a single pixel, $E_1 = E$, $E_2 = E \oplus E$, $E_3 = E \oplus E \oplus E, \ldots$ We are assured that E_{k+1} is E_k-open since $E_{k+1} = E_k \oplus E$ and the dilation of two sets is open with respect to both. Another, less elegant, way to form a satisfactory sequence of structuring elements is to simply construct the desired sequence "by hand".

As an illustration consider Fig. 1a, in which digital "balls" of four sizes are randomly dispersed about the image. The generating sequence $\{E_k\}$, from which the four balls generating the image are drawn, consists of digital balls of increasing size (the first being a single pixel). As ever larger balls are employed for the opening structuring elements, the grains (balls) in the image are sieved from the image. As the structuring element sequence passes each of the four balls that generate the image, translates of the specific structuring element are sieved from the image, the result being the unnormalized size distribution in Fig. 2a. Also shown in Fig. 2 are the normalized size distribution and the pattern spectrum (derivative). As opposed to the situation represented by the simulated image of Fig. 1, in many real world images, grains overlap to create larger, irregular compound grains that are not so regularly sieved by the granulometry.

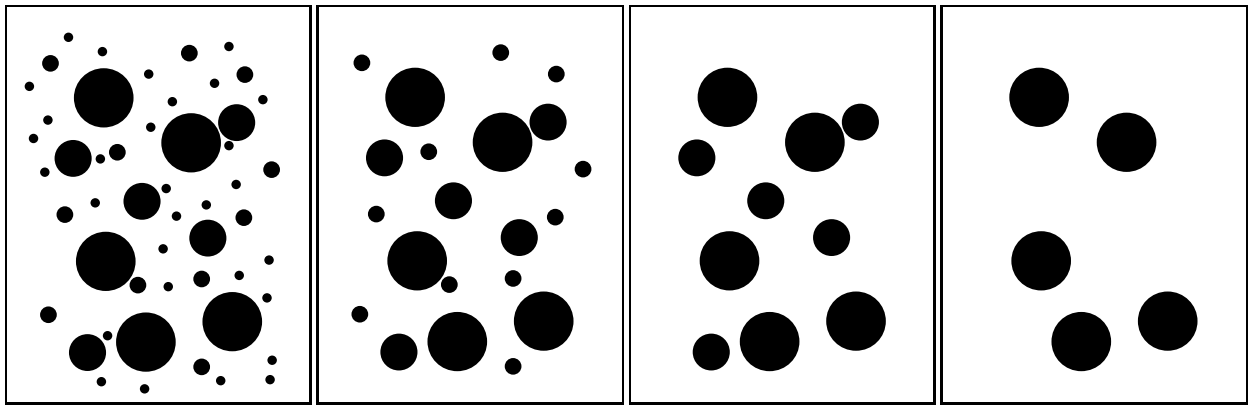

Figure 1: Binary image of discs (a) and its openings with respect to discs of increasing size ((b) to (d)).

While granulometries can be employed to describe shape [32, 38], more directly related to texture segmentation is their ability to measure changes in surface condition [8] and in particle distribution processes,

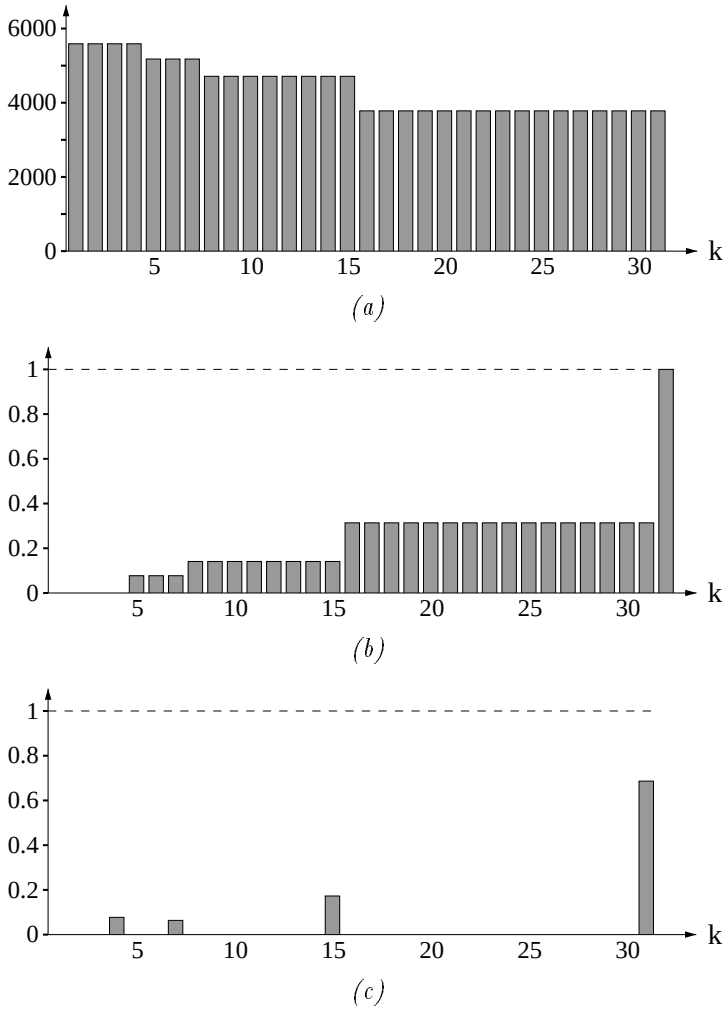

Figure 2: *(a) Size distribution $\Omega(k)$, (b) normalized size distribution $\Phi(k)$, and (c) pattern spectrum $d\Phi$ corresponding to the binary image of fig. 1a.*

for instance electrophotographic images [19]. Fig. 3 shows different examples of binarized particle distributions resulting from an electrophotographic process. In Fig. 3a the toner particles are fairly uniformly spread across the image, whereas in Fig. 3b the particles suffer from agglomeration, a typical problem with electrophotographic processes. Yet a different case is shown in Fig. 3c. Granulometries have been applied to these three images using a digital ball generating sequence, and the resulting pattern spectra are shown in Fig. 4. Notice how the agglomeration has resulted in a shift of the pattern spectra to the right, especially with regard to skewing to the right. We might expect this to result in significant changes in the mean, variance, and skewness of the pattern spectrum. In fact, hypothesis tests can be based on these granulometric moments to determine whether, owing to agglomeration (or some other problem), the electrophotographic process is out of control [19]. Indeed, from a statistical perspective, a captured toner particle image represents only a single selection from the population of images being generated by the electrophotographic process. Each captured image is only a realization of the process, and it is the overall random image process that is of concern.

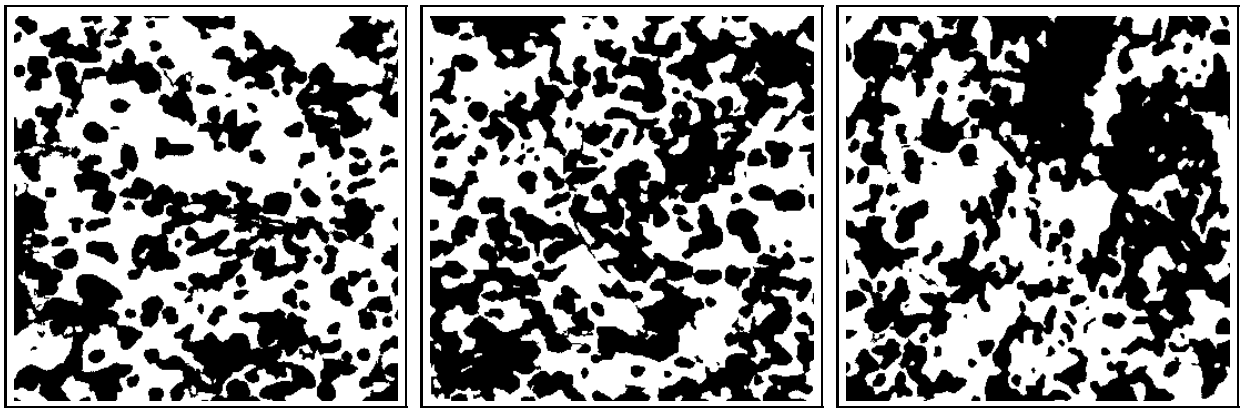

Figure 3: *Different examples of particle distributions resulting from an electrophotographic process.*

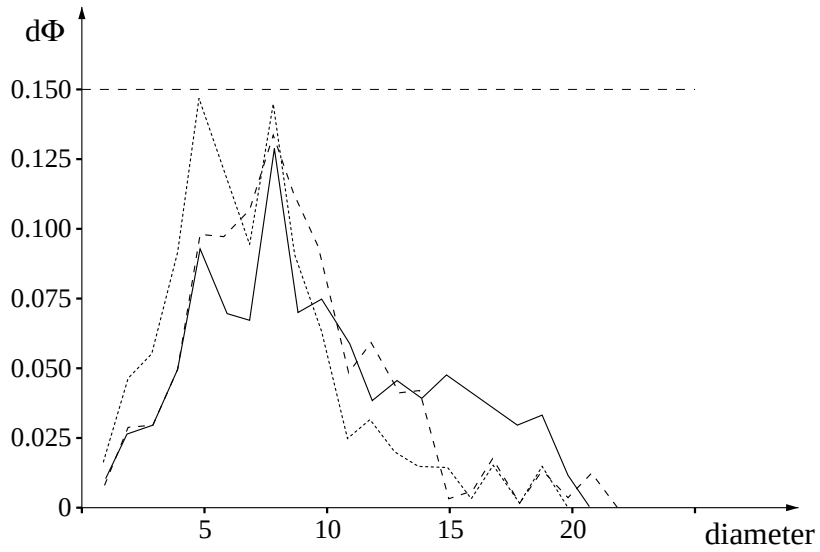

Figure 4: *Pattern spectra corresponding to Figs 3a–c.*

2.2 Granulometries on Random Binary Images

Owing to the randomness of the image process, the pattern spectrum is actually a random function (stochastic process). Each realization of the image process yields its own particular pattern spectrum, which is a realization of the spectrum process, and each spectrum realization has its own particular moments. Thus, the moments of the pattern spectrum (its mean, variance, skewness, etc.) are themselves random variables. Since these pattern spectrum moments are random variables, they possess their own statistical distributions, and these in turn possess their own moments. Thus, we arrive at the moments of the moments. Letting PSM, PSV, and PSS denote the mean, variance, and skewness of the pattern spectrum, PSM, PSV, and PSS are random variables possessing their own distributions. They have their own means (expectations) $E[PSM]$, $E[PSV]$, and $E[PSS]$, and their own variances, $Var[PSM]$, $Var[PSV]$, and $Var[PSS]$. Granulometric classification depends on the distributions of the pattern spectrum moments.

To illustrate the random model, we consider randomly placing $N = 50$ squares whose edge lengths are randomly chosen from a normal distribution with mean $\mu = 20$ and variance $\sigma^2 = 5$. In one case randomness of location is constrained so that the squares do not touch (nonoverlapping case) and in the other case there is no constraint on location (overlapping case). Realizations of the processes are shown in Fig. 5 and the pattern spectra for the depicted realizations are shown in Fig. 6. In all, 30 realizations have been performed for each case. For the nonoverlapping realizations the PSMs ranged from 20.0906 to 21.1104, with an average PSM of 20.4828. Taking the usual statistical approach, we take 20.4828 as an estimate of $E[PSM]$. The PSVs for the 30 nonoverlapping realizations ranged from 3.0565 to 7.6976, the average PSV being 5.0759. For the overlapping realizations, average PSM was 20.7614 and average PSV was 5.3515, these being taken as estimates of $E[PSM]$ and $E[PSV]$, respectively. Note that overlapping has slightly shifted the mean to the right.

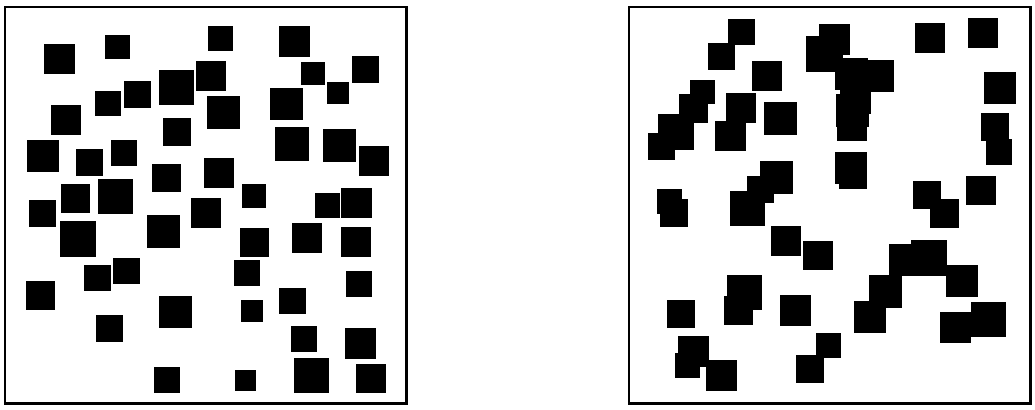

(a) non-overlapping *(b) overlapping*

Figure 5: Randomly generated images of squares.

The preceding example brings to focus a fundamental task of granulometric analysis: Given an image model, one would like to:

1. find expressions for the pattern spectrum moments,
2. find expressions for the moments of the pattern spectrum moments,
3. if possible, describe the statistical distributions of the pattern spectrum moments.

Generally, these problems are quite difficult and they have only been solved in some special cases [20, 42, 43, 2, 1]. We shall briefly consider one of these and merely mention another.

Consider a random Euclidean image process S whose realizations are disjoint unions of N scalar multiples of a single convex, compact primitive B:

$$S = (r_1 B + x_1) \cup (r_2 B + x_2) \cup \ldots \cup (r_N B + x_N) \tag{5}$$

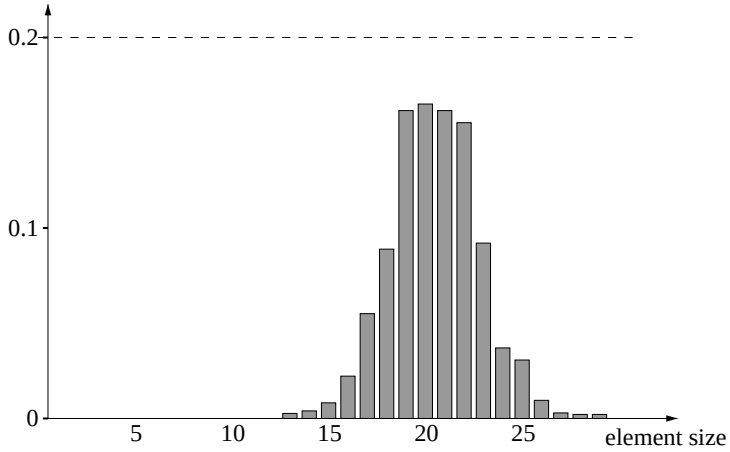

(a)

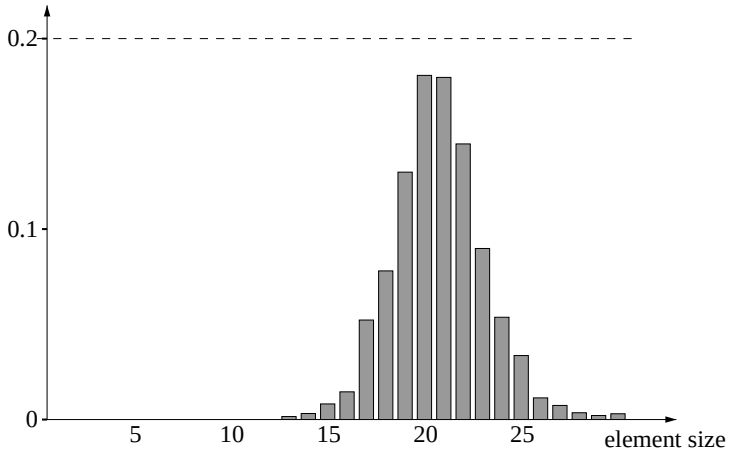

(b)

Figure 6: Pattern spectra corresponding to Figs. 5a and 5b.

where $r_iB + x_i$ is the translate of r_iB by x_i. S is random owing to both the locations (x_i) of the grains and the size (r_i) of the grains. Key to granulometric analysis is the sizing distribution governing $r_1, r_2, \ldots, r_N$. Under the model of Eq. (5), the kth central moment of the pattern spectrum for S generated by the primitive B is given by the random variable Z_{k+2}, where

$$Z_p = \frac{\sum_{i=1}^{N} r_i^p}{\sum_{i=1}^{N} r_i^2} \tag{6}$$

[20, 42, 43]. For instance, $PSM = Z_3$ and $PSV = Z_4 - Z_3^2$. In fact, other image models besides that of Eq. (5) possess granulometric moments given by Z_{k+2} and any grain model whose granulometric moments are given by Z_{k+2} is said to be *perfect* [42, 43].

If an image process is perfect, then it is possible to ascertain exactly the moments of its pattern spectrum moments [43]. More practically beneficial, under the assumption that the grain sizes are independent, it can be shown that the distributions of the pattern spectrum moments are asymptotically normal (with N) and that asymptotic expressions for the means and variances of the pattern spectrum moments can be obtained [42], so that the pattern spectrum moments are fully (asymptotically) described. For PSM and PSV asymptotic convergence is $O(N^{-1})$ and $O(N^{-3/2})$, respectively.

For instance, if the the sizing distribution is normal with mean μ and variance σ^2, then PSM is asymptotically normal with asymptotic mean

$$E[PSM] = \mu[1 + 2(1 + \mu^2\sigma^{-2})^{-1}] + O(N^{-1}) \tag{7}$$

and asymptotic variance

$$Var[PSM] = \frac{\sigma^2(\mu^8 + 8\mu^6\sigma^2 + 12\mu^4\sigma^4 + 12\mu^2\sigma^6 + 15\sigma^8)}{N(\sigma^2 + \mu^2)^4} + O(N^{-3/2}) \tag{8}$$

For the nonoverlapping process whose realization is depicted in Fig. 5a, the asymptotic value for $E[PSM]$ is 20.5000, which is very closed to the estimated value of 20.4828. For PSV, the asymptotic mean is

$$E[PSV] = \frac{\sigma^2(3\sigma^4 + \mu^4)}{(\sigma^2 + \mu^2)^2} + O(N^{-1}) \tag{9}$$

(see [42] for the asymptotic expression for $Var[PSV]$ with a normal sizing distribution and for asymptotic expressions for a gamma sizing distribution).

In addition to the perfect grain model, which applies to noisefree random images, granulometric moments have been studied for arbitrary deterministic, digital binary images corrupted by either union or subtractive white noise. Because the noise is random the pattern spectrum moments are random. Expressions have been found for the means of the first (PSM) and second pattern spectrum moments in the case of granulometries generated by linear structuring elements [2, 1].

2.3 Local Granulometric Size Distributions and Texture Analysis

The image process of Eq. (5) is homogeneous in that its statistical description is invariant across the image frame. As a texture process, its realizations represent the same texture and this texture occupies the entire image frame. More generally, we can consider an image process S defined on a frame F in such a manner that the frame is partitioned into n subframes,

$$F = F_1 \cup F_2 \cup \ldots \cup F_n \tag{10}$$

with F_i and F_j disjoint if $i \neq j$. Furthermore, suppose that, when restricted to F_i, S is defined by the image (texture) process T_i and that, for $i \neq j$, T_i and T_j are not identically distributed. Then S is composed of textures from the class $\mathcal{T} = \{T_1, T_2, \ldots, T_n\}$ and the domain of T_i is F_i. The segmentation problem is to observe a realization (or realizations) of S and estimate the regions $F_1, F_2, \ldots, F_n$. Using a pixel-based approach, the task is to associate a feature descriptor with each pixel and then classify the pixel into one of the regions according to the value of the observed descriptor. Since classification is to be texture-based

and since texture is regional, the feature descriptor at a pixel x must be a function of some neighborhood (window) containing x.

In the classical global approach to granulometries, the entire image is successively opened and at each stage an image pixel count is taken. To measure image texture local to a given pixel, rather than take the pixel count across the whole image we take the count in a window W_x about the pixel x.

Definition 3 (Local granulometric size distribution) *Consider a granulometry $\{A \circ E_k\}$ and an origin-centered window W. The local size distribution $\Omega_x(k)$ at pixel x generated by the granulometry is obtained by counting the number of pixels of $A \circ E_k$ in the translated window $W_x = W + x$ for each k. Normalization according to Eq. (2) yields a local granulometric size distribution $\Phi_x(k)$ and differencing yields a local pattern spectrum density $\Phi'_x(k)$.*

Each local pattern spectrum possesses moments. If a subregion of the image possesses homogeneous texture, then it is likely that the moments remain somewhat stable across the subregion and different subregions characterized by different textures can be differentiated based upon the local pattern spectrum moments.

If, for the moment, we confine ourselves to the mean, then for each pixel x we have a mean PSM_x and pixel regions are segmented based upon differing PSM_x values. According to the random process model, each PSM_x is a random variable and segmentation accuracy depends upon the probability distributions of the PSMs across the various texture regions.

The partition of Eq. (10) induces a secondary partition based upon the window W, which can be treated as a binary structuring element, namely,

$$F = \left(\bigcup_{i=1}^{n}(F_i \ominus W)\right) \cup \left(F \setminus \bigcup_{i=1}^{n}(F_i \ominus W)\right) \tag{11}$$

We write this new partition as

$$F = F_h \cup F_b \tag{12}$$

If $x \in F_h$, then there exists i such that $W_x \subseteq F_i$; if $x \in F_b$, there does not exist such an i. Thus, for $x, y \in F_h$, if x, $y \in F_i \ominus W$, then PSM_x is identically distributed to PSM_y; if x and y do not lie in the same region, then PSM_x and PSM_y are not identically distributed. Segmentation of the subregions of F_h results from observing the local PSM values. As for the residual region F_b, pixels within it have windows lying in more than a single texture region and therefore the local PSMs at these pixels result from mixed processes. Typically, these PSMs are also used for classification; however, estimation accuracy suffers. F_b is composed of border regions and the size of these regions is a function of window size. A small window size decreases the size of the border regions, but at the same time a small window tends to decrease the accuracy of estimation within regions because it makes the PSMs more susceptible to realization fluctuation [20].

As an illustration, consider the realization of Fig. 7a, in which each side of the image consists of randomly dispersed balls possessing random radii, the difference being that on the right side the mean radius is smaller than that on the left side. Using local granulometric size distributions generated by a ball and then segmenting based upon the local pattern spectra means yields the segmented image in Fig. 7b. Here, the method of segmentation is quite straightforward: since there are only two regions, the local PSMs are computed and those above a certain threshold are considered to arise from pixels on the left, while the others are considered to arise from pixels on the right. Two points should be noted. First, a single grain approach will not work because, owing to size randomness, grains resulting from the larger sizing distribution can be smaller than grains resulting from the smaller sizing distribution. Second, owing to overlapping, grains in the small size region can cluster and thus be seen as forming a large grain region, and, owing to random location, there can be gaps in the large grain region that result in pixel misclassification into the small grain region. At least insofar as the classification of Fig. 7a is concerned, these misclassifications can be mitigated by performing an opening followed by a closing with a relatively small ball, the only cost being a slight smoothing of the classification boundary.

Generally, one requires more features than merely the local PSM to classify a pixel; variances and other higher order pattern spectrum moments might be necessary. The choice of structuring element sequence is also important; in fact, good segmentation will likely require a number of local size distributions generated

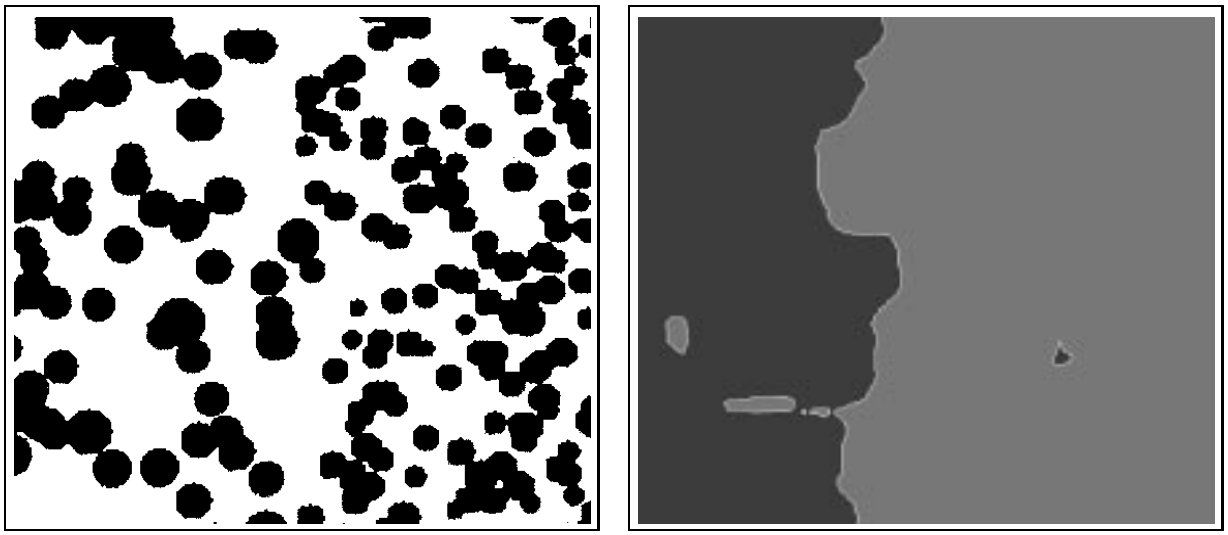

(a) original image *(b) segmented image*

Figure 7: Texture segmentation via local pattern spectra means.

by various structuring element sequences. An example of such a situation occurs in Fig. 8a. A ball sequence can separate the thick rectangles and balls from the thin rectangles and a vertical linear sequence one pixel wide can separate the rectangles from the balls. Using the local pattern spectra resulting from each of these sequences in conjunction yields the segmented image of Fig. 8b. Segmentation has been accomplished by forming two partially segmented images, the balls and thick rectangles from the thin rectangles and the rectangles from the balls, and then logically operating to obtain the final segmentation.

The image of Fig. 9a illustrates a different problem. We wish to employ a ball generated sequence to segment the left side from the right. The local pattern spectra on the left tend to be spike like and centered at the common ball radius; the local pattern spectra on the right tend to possess two spike-like concentrations centered at the two radii of the balls composing that side of the image. In both regions, the local PSMs cluster around the common ball radius of the left side. Hence, local PSMs cannot achieve segmentation. However, segmentation can be achieved via local PSVs, since the local PSVs on the left are close to zero, whereas the local PSVs on the right reflect two-spiked local pattern spectra. The segmentation shown in Fig. 9b results from classifying together all pixels with PSV above a certain threshold, these composing the right side of the segmentation.

More generally, segmentation of real world images requires application of statistical classification methods to local pattern spectrum moments. The general approach can be described via the texture family $\mathcal{T} = \{T_1, T_2, \ldots, T_n\}$. If $x[i]$ is an arbitrary pixel in region $F_i \ominus W$, so that $W_{x[i]} \subseteq F_i$, for a given granulometry there is a local pattern spectrum associated with $x[i]$, which, as a random function, is identically distributed with the local pattern spectrum for any other pixel in $F_i \ominus W$. This local pattern spectrum possesses moments, in particular, PSM_i, PSV_i, and PSS_i, so that we can associate the random feature vector $\vec{F}_i = (PSM_i, PSV_i, PSS_i)$ with $x[i]$, or, more generally, with F_i. In fact, as evidenced by a preceding example, we might need to employ more than a single granulometry. If we employ m different granulometries, then $\vec{F}_i$ will have $3m$ component features.

Pixel classification is accomplished in the following manner. Assume we know the multivariate probability distribution of $\vec{F}_i$ for $i = 1, 2, \ldots, n$. If we then observe a realization of the image process and select a pixel x, the same granulometric features that compose the feature vectors $\vec{F}_i$ are computed locally for x and this results in a feature vector $\vec{F}_x$. By employing some statistical measure of closeness, a determination is made as to which feature vector, $\vec{F}_1$, $\vec{F}_2$,..., or $\vec{F}_n$, the observed vector $\vec{F}_x$ is closest. If $\vec{F}_x$ is closest to $\vec{F}_i$, then x is classified into region F_i (classified as belonging to a texture region of the type T_i). Application of the method depends on a choice of classification methodology. The method thus far employed has been Gaussian maximum likelihood classification [18].

A number of questions arise regarding granulometric texture classification. Two important ones having

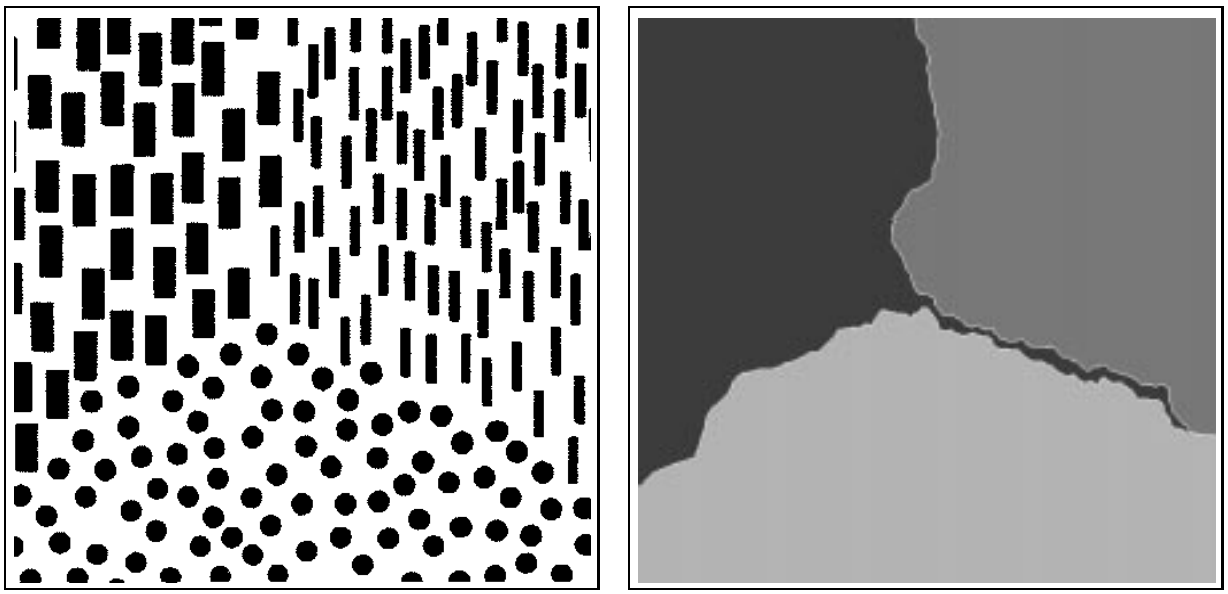

(a) original image *(b) segmented image*

Figure 8: Segmentation of tri-phased binary texture.

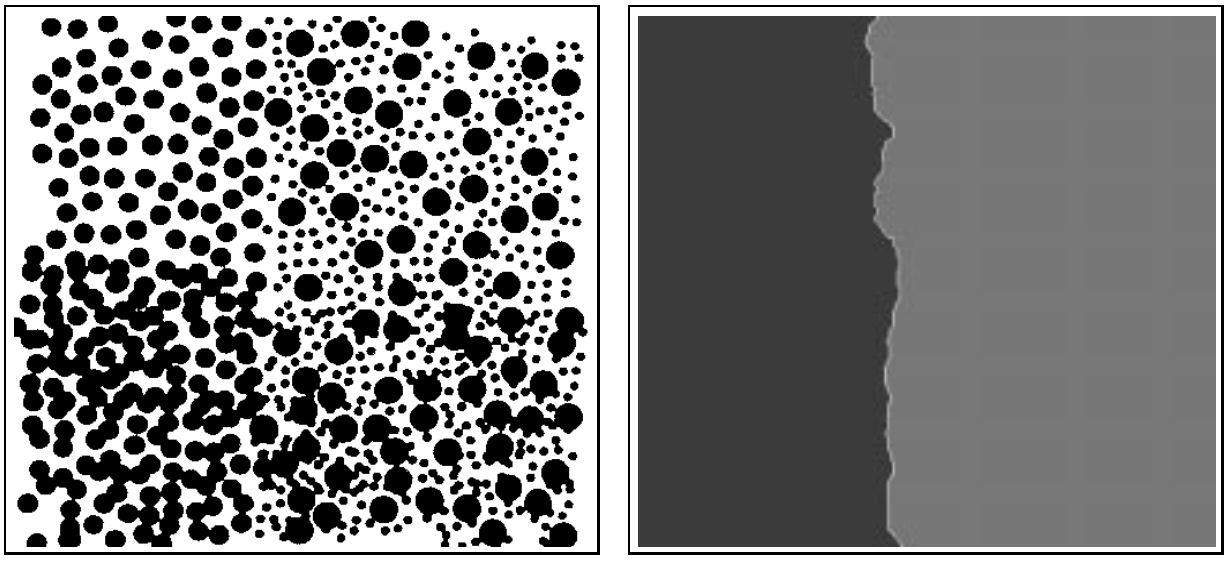

(a) original image *(b) segmented image*

Figure 9: Texture segmentation via local pattern spectra variances.

been addressed [18] concern robustness and classifier minimization. First, the method is quite robust with respect to certain types of union noise. This should be expected since openings filter out union noise and, so long as the noise components are sufficiently small, we should expect them to be filtered out early in the granulometric process. In addition, training in noise has been seen to be quite beneficial. Regarding classifier minimization, although we might initially employ a large number of granulometric features, many might be redundant and, worse yet, some might actually confuse the classification process. Moreover, large feature sets require large computation times. In [18], feature sets have been greatly reduced via a minimization procedure; indeed, very high accuracy has been achieved for the texture class under study there by using only six features.

2.4 General Granulometries

Thus far we have considered only the most basic granulometries, those generated by a single primitive generator. The present subsection describes Matheron's general theory of binary granulometries [34].

Definition 4 (Granulometry) *A granulometry is a collection of binary image operators* $\{\Psi_t\}$, $t > 0$, *such that (1)* Ψ_t *is antiextensive for all* t, *(2)* Ψ_t *is increasing for all* t, *and (3)*

$$\Psi_t \Psi_s = \Psi_s \Psi_t = \Psi_{\max\{t,s\}} \tag{13}$$

If we view t as a sieving parameter for sieves of increasing mesh size, we see the genesis of the three properties:

1. the image remaining after any sieving operation is a subset of the original
2. if one image is a subset of another, then the sieved images maintain the same subset relation
3. if Ψ_t and Ψ_s are two sieves in the process, the order of sieving does not matter, the remaining image being the same as if one were only to sieve through the largest of the mesh sizes.

Two further properties are deduced from the three basic postulates [34]: if $r \geq s$, then $\Psi_r(A) \subseteq \Psi_s(A)$, and the invariant class of Ψ_r is a subclass of the invariant class of Ψ_s. In line with the sieving model, there will be less residue remaining after sieving with the larger sieve, and those images that are invariant under the larger sieve must also be invariant under the smaller sieve.

The elementary opening granulometries $\{A \circ tB)\}$, B compact and convex, satisfy the three granulometric postulates. They also satisfy two other fundamental properties:

4. they are translation invariant
5. the following equation is satisfied:
$$\Psi_t(A) = \Psi_1(t^{-1}A) \tag{14}$$
for any $t > 0$ and any binary Euclidean image A.

Property 5 is the most interesting: it says that there is a *unit* sieve, Ψ_1, and that any other sieve in the process can be evaluated by first scaling the image by the reciprocal of the parameter, filtering by the unit sieve, and then rescaling. If one thinks of sieving particles through a mesh, the property appears quite intuitive.

Definition 5 (Euclidean granulometry) *If a granulometry* $\{\Psi_t\}$ *satisfies properties (4) and (5), then it is called a Euclidean granulometry.*

Every Euclidean granulometry can be expressed in terms of openings [34], an elementary opening generated by a convex, compact primitive being the simplest Euclidean granulometry. While we leave a full discussion to more complete texts [17, 23], we note that the most important example of a Euclidean granulometry is a finite union of openings, each by a parameterized convex, compact primitive:

$$\Psi_t(A) = (A \circ tB_1) \cup (A \circ tB_2) \cup \ldots \cup (A \circ tB_n) \tag{15}$$

The set of primitives $\mathcal{B} = \{B_1, B_2, \ldots, B_n\}$ is called the *generator* of the granulometry and the invariant class of Ψ_t is composed of all binary images that can be formed as unions of translates of scalar multiples tB_i of B_i where $t \geq 1$. The key to the relative simplicity of Eq. (15), as opposed to more complicated Euclidean granulometries, is that the generator is composed of convex shape primitives. In effect, rather than construct granulometric size distributions by utilizing a single convex shape primitive, one examines the sieving effect by a generator consisisting of several convex shape primitives. Like single-primitive granulometries, more general granulometries induce size distributions.

As in the case of a granulometry generated by a single primitive, some care must be exercised when going to the digital setting. Since the Euclidean property, Eq. (14), is not applicable in the digital setting, we content ourselves with satisfying the first four properties. Consequently, for digital images we employ granulometries of the form

$$\Psi_k(S) = (S \circ E_{1k}) \cup (S \circ E_{2k}) \cup \ldots \cup (S \circ E_{nk}) \tag{16}$$

where, for $j = 1, 2, \ldots, n$, $E_{j,k+1}$ is $E_{j,k}$-open.

It is interesting to note that the asymptotic methods of [42] apply to multiply generated Euclidean granulometries of the form given in Eq. (15) if the primitives composing the generator possess the *orthogonality* property defined therein; that is, under the condition of generator orthogonality, the granulometric moments are asymptotically normal and asymtotic expressions for the means and variances of the moments can be derived.

2.5 Extensions of Granulometric Texture Classification

Two extensions of the granulometric approach to texture classification deserve mention: (1) granulometries employing the image complement and (2) grayscale texture analysis.

If we consider the image frame F as a binary image, then, given an image A, we can treat the set subtraction $F \setminus A$ as a complementary image (also denoted A^C). If A represents the foreground, then $F \setminus A$ represents the background. Granulometries of the type $\{A \circ tB\}$ provide information via filtering from the inside of A; we can also consider granulometries of the type $\{(F \setminus A) \circ tB\}$. These complementary granulometries provide information via filtering the complement of A. Pattern spectra moments formed from granulometries on $F \setminus A$ can be used to augment those formed from granulometries on A.

Binary and grayscale openings share the same definition in terms of erosion and dilation, and whereas the binary opening of set A by structuring element B is given by the union of all translates of B that are subsets of A, the grayscale opening of a function f by a structuring element (function) g is given by the supremum of all grayscale translates of g that lie beneath f. Like binary openings, grayscale openings possess four fundamental filter properties: translation invariance, increasing monotonicity, antiextensivity, and idempotence. Furthermore, Matheron's Euclidean granulometric theory extends to grayscale signals [21] and granulometric size distributions can be constructed for texture analysis.

These grayscale granulometries have been used, for example, to detect the presence of osteoporosis in magnetic resonance (MR) images [15], as illustrated by Fig. 10. Fig. 10a shows an MR image of a wrist bone, the bone itself horizontally traversing the upper half of the image. The trabecular structure of the bone appears as a grainy texture and osteoporosis is evidenced by diminished trabecular structure. Grayscale granulometric features have been employed to classify bone pixels: the osteoporotic region of the bone extracted by the classifier is outlined in Fig. 10b. Note that, even though the extracted region extends beyond the bone, only pixels within the bone region have been classified. Refer to [15] for details.

In analogy to [18], texture classification via grayscale granulometric moments has been studied in the context of Gaussian maximum-likelihood classification [13, 14]. The effects of employing complementary granulometries, recognition in noise, training in noise, and Karhunen-Loeve feature reduction have been investigated.

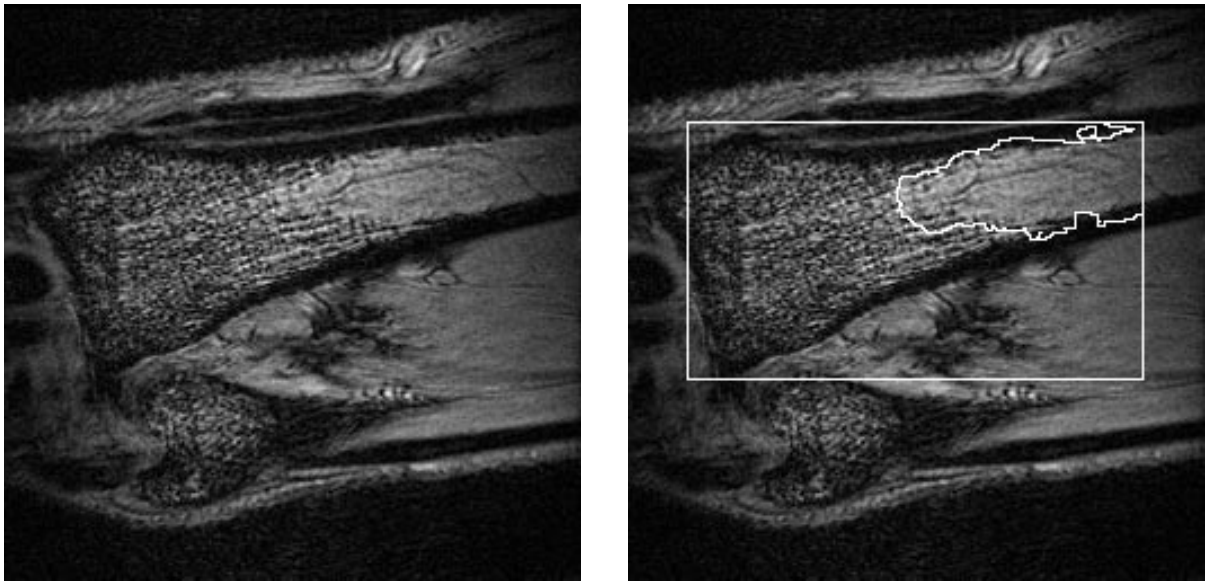

(a) original image *(b) segmented image*

Figure 10: Granulometric segmentation of grayscale MR images of osteoporetic bone regions.

3 Binary and Grayscale Particle Segmentation

3.1 Introduction

As previously mentioned, the purpose of this section is to show how morphology can be successfully applied to a wide range of object segmentation problems. In this section, *segmentation* of an image refers to the task consisting in extracting from it the objects or particles of interest as precisely as possible. By region-contour duality, this is equivalent to dividing the image in object regions and background regions.

Segmenting an image I is more than simply counting its objects and pointing at them in the image: it also encompasses the extraction of the objects' contours. However, as we shall repeat throughout this section, the contour extraction step usually requires the prior *marking* of the objects to extract. By a *marker* of an object or set X, we simply mean a set M that is included in X. We also generally assume that markers have the same *homotopy* as the set they are marking. For example, a marker of a connected set is usually connected itself, although this constraint can in fact be loosened in many practical cases. Moreover, markers are usually located towards the central part of the objects they mark.

This marker extraction step is shown to be the most important step in many complex segmentation applications that are undertaken using morphology. Intuitively, this marking is an algorithmic simulation of human behavior: when asked to show the objects present in an image, a human does not start right away by precisely outlining these objects. On the contrary, he or she will first point at the objects, one after the other, thus marking them. This marking can be seen as a first estimate of the objects; it is then refined by outlining the object's contours. From an image analysis point of view, it is generally admitted that finding object markers is a less difficult task than directly extracting accurate contours. In this section, we show that going from markers to actual segmentation can be done automatically using procedures that we will describe, and that are mainly based on the watershed transformation.

In the binary case, segmentation refers to the extraction of the connected components representing objects of interest, as well as the separation of the overlapping objects. For example, the binary image shown in Fig. 11a represents coffee beans. This image will be used throughout this section to illustrate the effect of the morphological transformations we will be dealing with. We can count the beans present in the image by simply extracting a connected marker for each bean and counting the number of markers. However, this is not sufficient if one wishes to perform measurements on each individual bean (area, perimeter, elongation,

etc). For this purpose, the beans need to be segmented, i.e. separated from one another. In the following, binary segmentation means "separation of overlapping objects in a binary image".

This marker-based methodology will also provide a framework for grayscale segmentation. We will illustrate our approach on the ultra-classic image of 2-D electrophoresis gels shown in Fig. 11b. On this image, we not only want to find all the dark spots, but also correctly outline them in order to measure, e.g., their respective areas, the density of black under them, etc. In both the binary and the grayscale segmentation cases, the *watershed transformation* (see section 3.4) will be used to extract precise object outlines from markers. We will talk about *marker-driven watershed segmentation.*

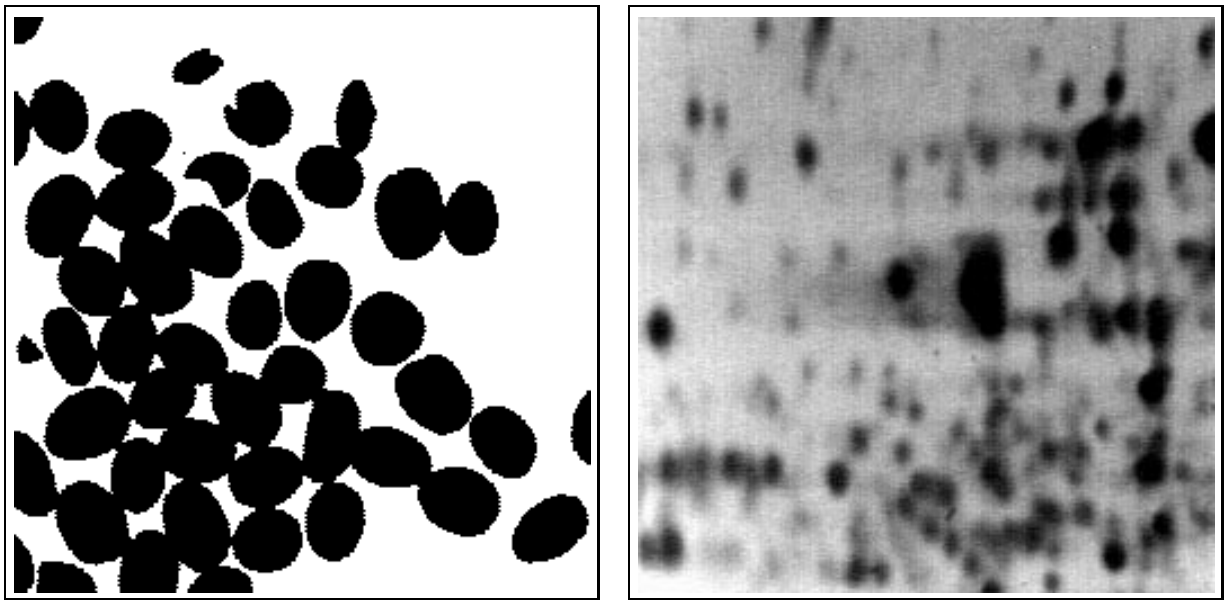

(a) *(b)*

Figure 11: (a) binary image of coffee beans that need to be separated; (b) grayscale image of 2-D electrophoresis gel whose spots have to be extracted.

Note that in many simpler cases, there is no need to apply this approach. For example, the *top-hat* transformation originally proposed in [36] provides an excellent tool for extracting light (resp. dark) objects from an uneven background. Its relies on the fact that by grayscale opening, one removes from an image the light areas that cannot hold the structuring element. Subtracting the opened image from the original one yields an image where the objects that have been removed by opening clearly stand out, and that image can then easily be thresholded (see Fig. 12).

Archetypically, the structuring element used in the opening step is a disk or a discrete approximation of a disc. However, infinite variations of this transformation can be derived. We may cite:

- using linear elements, one can specifically extract objects that are elongated in one direction,
- using a closing instead of an opening and subtracting the original image from the closed one allows us to extract dark objects on a lighter background. In this case, we talk about "black top-hat" as opposed to the "white top-hat" (by opening).
- If the background contains a lot of thin and elongated objects, one can use maxima of openings (resp. minima of closings) with linear elements, followed or not by grayscale reconstruction (see section 3.3.4), or area openings (resp. closings) [55].

An application is shown in Fig. 13: Fig. 13a is a scanning electron microscopy image where the balls in the lower right corner are to be extracted. These being compact and light compared to the background around them, they are removed by an opening of size 2 (see Fig. 13b). After subtraction of (b) from (a), i.e. top-hat (see Fig. 13c), these small balls stand out and this image can be easily thresholded into Fig. 13d.

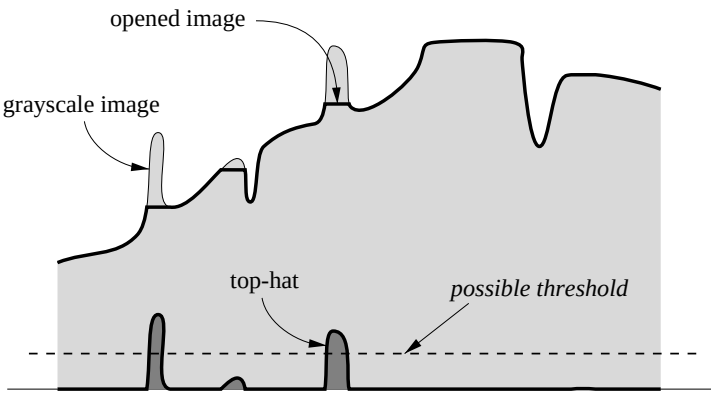

Figure 12: Peaks extracted via top-hat followed by thresholding.

The desired balls (right side) can now be extracted as the balls contained in the largest connected component of the dilation of Fig. 13d. The dilated image is shown in Fig. 13e, and the resulting segmentation is shown in Fig. 13f.

In the following, we concentrate on more complex segmentation problems, where top-hats cannot provide satisfactory solutions. We first deal with binary segmentation, and the tools and techniques we are lead to use turn out to be even more useful later, for grayscale segmentation. In section 3.2, we present the concepts of maximal balls and skeletons and show how they can be used to robustly mark the centroid of overlapping objects in binary images. To go further and, from these markers, derive the desired binary segmentation, we need to make use of *geodesic operators* that are defined in section 3.3. The grayscale version of these operators is also very useful for grayscale segmentation. Lastly, in section 3.4, we describe the watershed transformation in detail and show how it unifies both binary and grayscale segmentations. Its use is illustrated on the segmentation of images of 2-D electrophoresis gels.

Some reminders and notations

From this point on, we are only concerned with the discrete case, i.e., our workspace is the discrete plane $\mathbb{Z}^2$. In this plane, a *grid* G provides the neighborhood relationships between pixels. Commonly used grids are the square grid, for which a pixel p has either 4 (in 4-connectivity) or 8 neighbors (in 8-connectivity), as well as the hexagonal grid (6-connectivity). Two neighboring pixels p and q form an edge of G. The grid G induces a discrete distance in $\mathbb{Z}^2$, the distance between two pixels being the minimal number of edges required to join them.

Discrete images are considered as mappings from $\mathbb{Z}^2$ onto $\mathbb{Z}$; grayscale images take their values in a range $\{0, 1, \ldots, N\}$ whereas binary images can only take value 0 and 1. The information content of a binary image is contained in its pixels with value 1, and therefore, binary images are often regarded as sets. For this reason, the binary transformations described in the following are often defined as set transformations.

3.2 Maximal Balls, Skeletons, Ultimate Erosions

We have seen in section 2 that granulometric analyses allow one to extract size information about an image without the need to segment it. For example, consider the coffee bean image X shown in Fig. 11. Depending on the context, X shall either refer to the image itself or to the set of its black pixels. The granulometric analysis of this image may be undertaken using squares of increasing sizes, denoted S_1, S_2, etc: openings with the S_i's are thus performed for $i = 1$ to the first value n such that $X \circ S_n = \emptyset$. At each step i, the area of image $X \circ S_i$ is determined.

The $(X \circ S_i)_{0 \leq i \leq n}$ constitutes a decreasing sequence of sets, so that as shown in [57], one can synthesize all the information contained in this sequence via a single function called the *granulometry function.*

Definition 6 *The granulometry function g_X associated with a set X and the family of convex and homothetic*

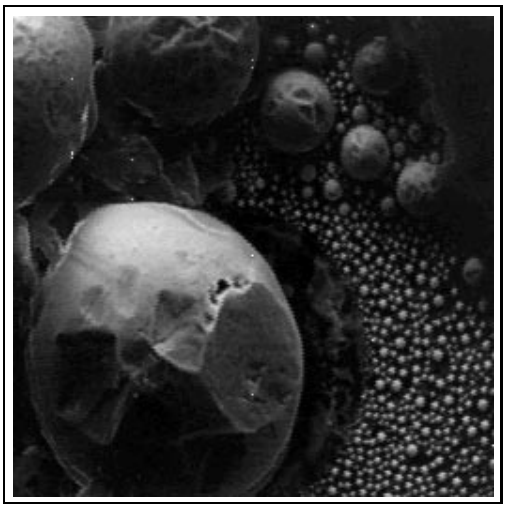

a. original image

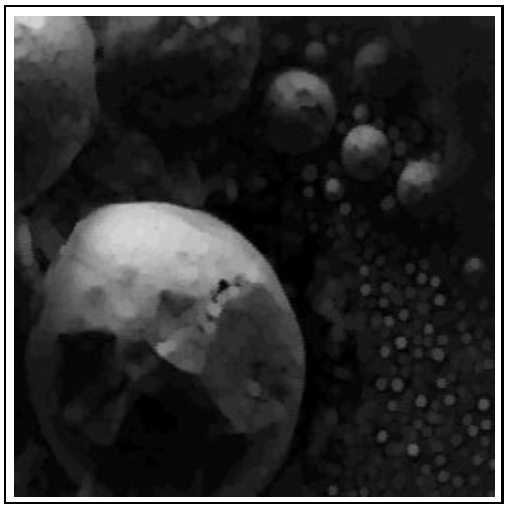

b. opening of with disc of radius 2

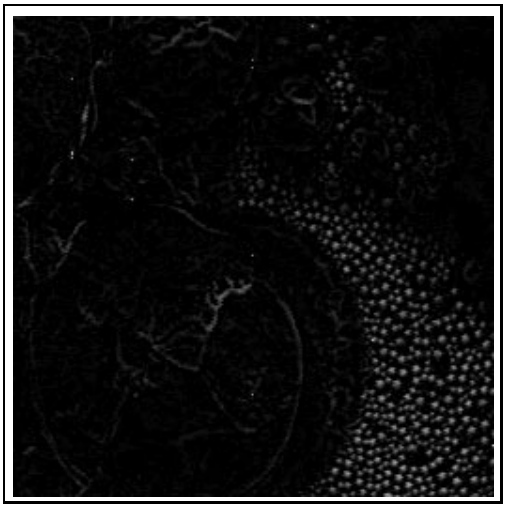

c. corresponding top-hat

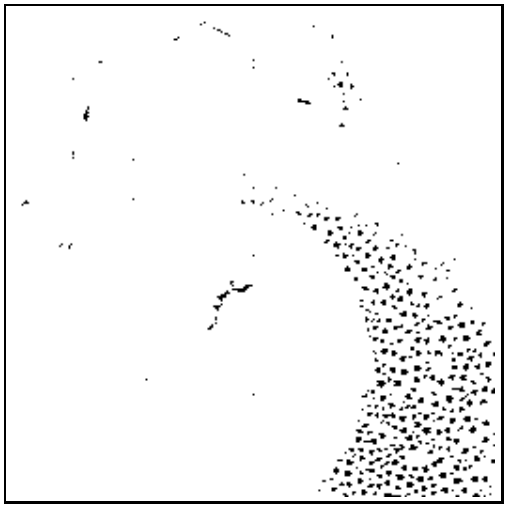

d. threshold

e. dilation of d

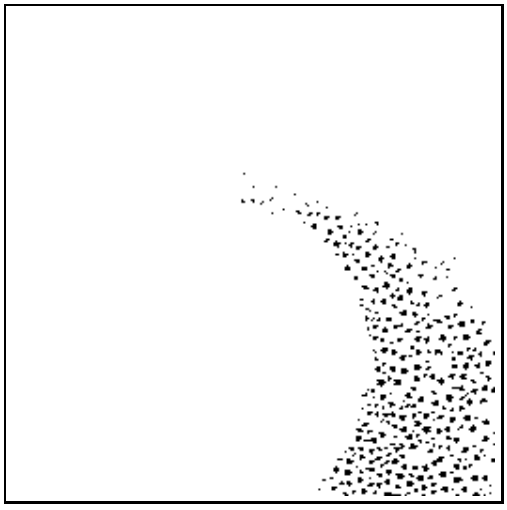

f. final result

Figure 13: Top-hat segmentation of SEM image.

elements $(S_i)_{i\geq 0}$ *maps each pixel of* X *to the first* i *such that* $x \notin X \circ S_i$*:*

$$g_X : p \in X \longmapsto \min\{i \in \mathbb{N}, p \notin X \circ S_i\}. \tag{17}$$

Alternatively, one can say that the granulometry function maps each pixel of X to the maximal i such that there exists a translation $t(S_i)$ of S_i satisfying $p \in t(S_i) \subseteq X$. The granulometry function of our coffee beans image is shown in Fig. 14.

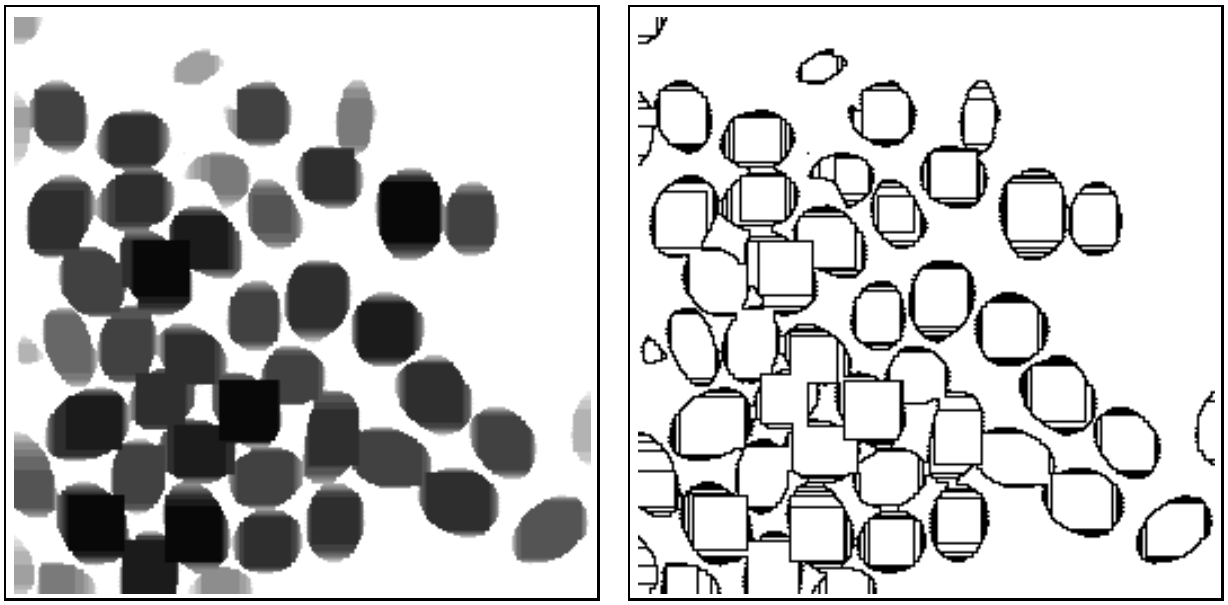

(a) *(b)*

Figure 14: (a) Granulometry function of Fig. 11a with respect to a family of squares; (b) level lines of this function.

From these images, it becomes clear that our coffee beans can be described as the areas where the largest balls (in this particular case: squares) can be included. Therefore, to extract markers of our beans, we shall start by looking at the image zones where the "largest" balls can be extracted.

3.2.1 Definitions

In this section and the following, the notion of *ball* directly stems from the distance being used. For example, in the plane $\mathbb{R}^2$ equipped with the usual Euclidean distance, the balls are standard discs. In the discrete plane $\mathbb{Z}^2$, the balls are hexagons if the hexagonal grid is used (6-connectivity) or squares in square grids. The unit size ball B (ball of radius 1) corresponds to either S_1, H or S_2 depending on whether 4-, 6- or 8-connectivity is used (see Fig. 15).

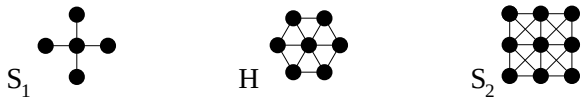

Figure 15: Unit size ball B in 4-, 6- and 8-connectivity respectively.

Calabi's definition of the skeleton is based on the following notion of maximal ball:

Definition 7 *A ball* B *included in* X *is said to be maximal if and only if there exits no other ball included in* X *and containing* B*:*

$$\forall B' \text{ ball}, \quad B \subseteq B' \subseteq X \Longrightarrow B' = B. \tag{18}$$

This concept is illustrated by Fig. 16, and the definition of the skeleton follows from it:

Definition 8 (Skeleton by maximal balls) *The skeleton S(X) of a set $X \subset \mathbb{Z}^2$ is the set of the centers of its maximal balls:*

$$S(X) = \{p \in X \mid \exists r \geq 0, B(p,r) \text{ is a maximal ball of } X\}. \tag{19}$$

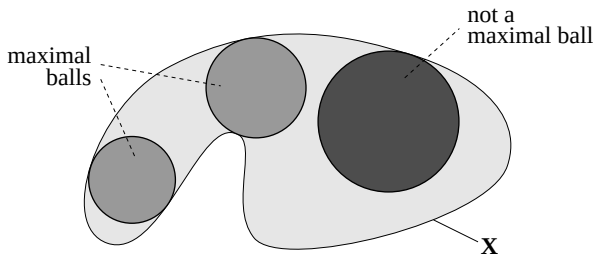

Figure 16: Concept of maximal ball in the Euclidean plane.

The skeleton is an intuitive notion: the skeleton of a ball is reduced to its center, that of a band yields a unit thickness line, etc. Examples of skeletons of simple shapes are shown in Fig. 17. One can see why the skeleton is often called the *medial axis transform:* it provides a description of sets in terms of lines of unit pixel thickness.

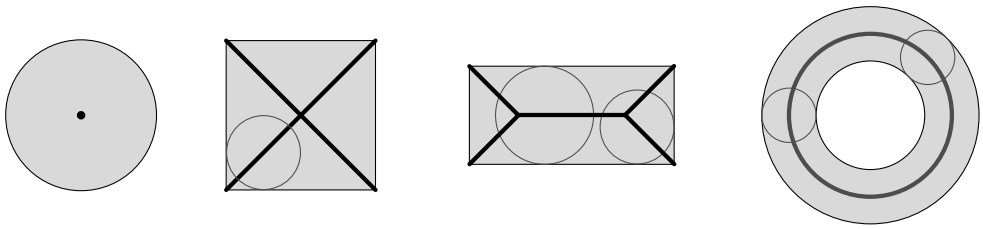

Figure 17: Skeleton of simple shapes in the Euclidean plane.

Unfortunately, things are not as easy as they look: in the continuous case (Euclidean plane $\mathbb{R}^2$), e.g., the skeleton of two tangent discs is reduced to the two centers of these discs (see Fig. 18) instead of being a straight line joining these two points. In other words, the *homotopy* or *connectivity* of the original set is not necessarily preserved (see [46, chapters 11–12] for more details).

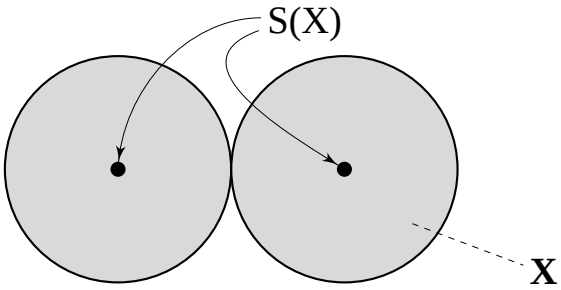

Figure 18: In the continuous Euclidean plane, the skeleton of a connected set is not necessarily connected.

In the discrete case, let us denote by nB the ball of radius n in the considered connectivity:

$$nB = \underbrace{B \oplus B \oplus \cdots \oplus B}_{n \text{ times}},$$

with B being equal to either S_1, H, or S_2. Lantuéjoul proved that the skeleton by maximal balls can be obtained by the following formula:

$$S(X) = \bigcup_{n=0}^{+\infty} [(X \ominus nB)/((X \ominus nB) \circ B)]. \tag{20}$$

In words, the skeleton by maximal balls can be obtained as the union of the residues of openings of X at all scales. Unfortunately, once again the skeleton does not behave as one would hope: the direct application of formula (20) yields completely disconnected skeletons, as illustrated by Fig. 19.

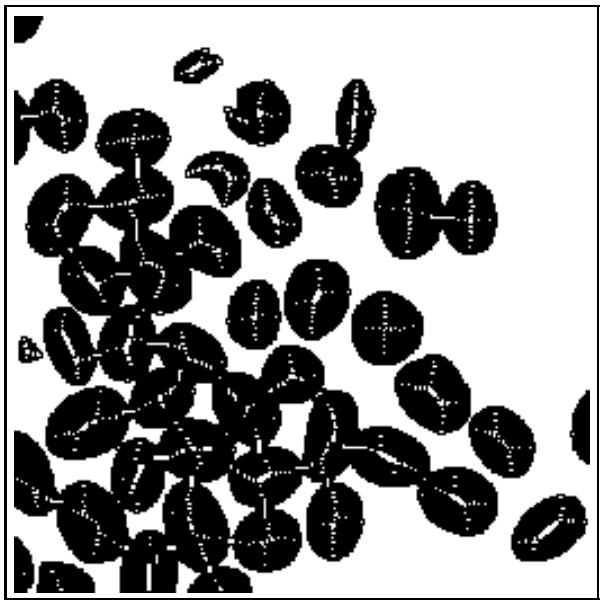

Figure 19: *Example of skeleton by maximal balls on the coffee beans image, using the balls of the 8-connected distance.*

Extracting correct homotopic (connected) skeletons from discrete binary images is thus not a straightforward matter. The literature on skeletons is very abundant and we certainly do not intend to cover the extraction of connected skeletons in this chapter. Let us just mention that the method recently proposed in [52] allows the very efficient computation of a connected skeleton which is a minimal superset of the skeleton by maximal balls. An example of a connected skeleton computed in 8-connectivity using this method is shown in Fig. 20a. Since the skeleton by maximal balls is not necessarily of unit-pixel thickness, the connected skeleton of Fig. 20a is not either. For some applications, it can be of interest to use thinning techniques to reduce it to a single pixel thickness, as shown in Fig. 20b.

3.2.2 Quench Function

Let us go back to our description of binary sets in terms of maximal balls and see what more can be said about these descriptions. By definition, to every pixel p in the skeleton, there corresponds a maximal ball. Let us denote by $q_X(p)$ the radius of this ball. We thus define the *quench function*

Definition 9 (Quench function) *The quench function associates with every pixel $p \in S(X)$ the radius of the corresponding maximal ball.*

One of the most important results about the quench function is that its datum is sufficient to reconstruct the original set completely:

Theorem 10 *A set X is equal to the union of its maximal balls:*

$$X = \bigcup_{p \in S(X)} (p + q_X(p)B). \tag{21}$$

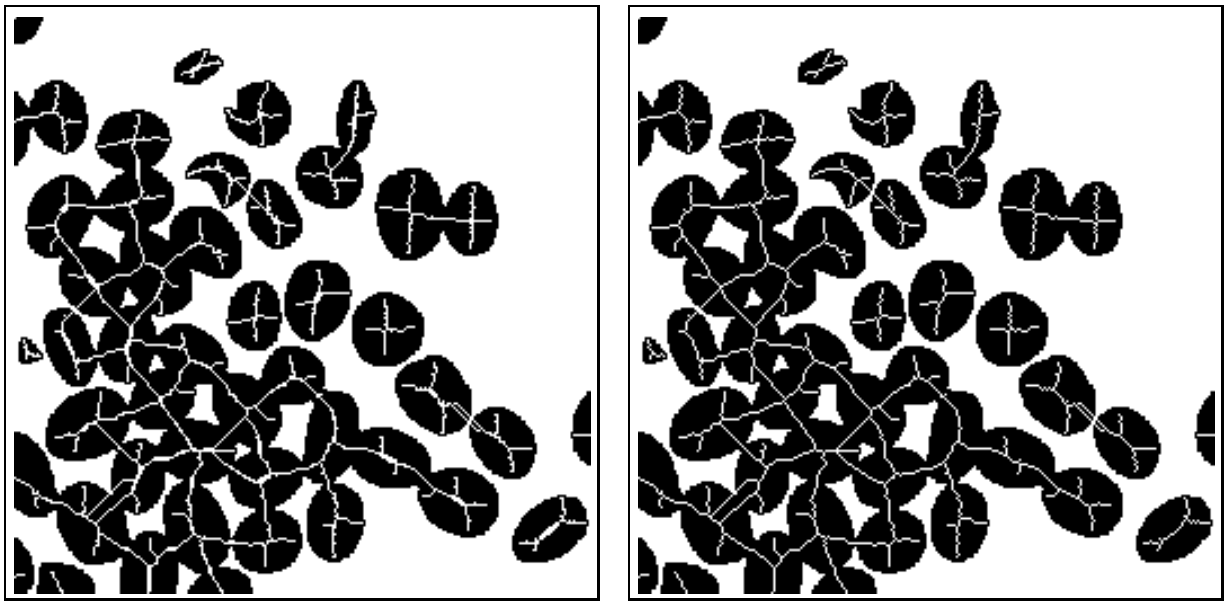

(a) *(b)*

Figure 20: (a) 8-connected skeleton; (b) thinned 8-connected skeleton.

The quench function thus allows us to do lossless encoding of binary images, and it has been extensively studied for image compression. Derived versions of this concept equal in performance the famous *CCITT group 4* encoding scheme on some kinds of document images [11].

The quench function of our image of coffee beans is presented Fig. 21a. Obviously, since this mapping is defined on the skeleton by maximal balls $S(X)$, its support is not connected. However, using the skeletonization technique briefly mentioned above [52], it is possible to re-connect the skeleton by maximal balls and to extract the radii corresponding to pixels on the connecting arcs. This produces the *connected* quench function shown in Fig. 21b.

The other major interest of the quench function is the definition of the *ultimate erosion.* We have now a way to describe a set X as the union of its maximal balls; in order to define markers of our coffee beans, i.e., of the convex blobs of the binary image under study, we look for the largest among these maximal balls. Clearly, for a given connected component C of X, (one of) the largest maximal ball is (one of) the largest ball that can be included in C, and its center marks an important object. However, if C is made of two overlapping objects, this crude method only allows us to mark one of them.

Let us consider the simple case where X is equal to the union of two overlapping discs. As shown on Fig. 22, the skeleton of X is the line segment joining the centers of these two discs. Now, upon examination of the quench function, one can notice that it exhibits two maxima, located at the exact centers a and b of our discs[1]. These maxima therefore define *markers* of our overlapping objects, and their set constitutes the *ultimate erosion* of X:

Definition 11 (Ultimate erosion) *The ultimate erosion of a set X, denoted Ult(X), is the set of the (regional) maxima of the quench function q_X of X.*

At this point, we need to recall the definition of *maxima* (also called *regional maxima*) for grayscale images:

Definition 12 (Regional maximum) *A regional maximum M of a grayscale image I is a connected component of pixels with a given value h (plateau at altitude h), such that every pixel in the neighborhood of M has a value strictly lower than h.*

One should make a clear distinction between *regional* maxima and *local* maxima. A local maximum is defined as follows:

[1] In this particular case, these maxima also happen to be located on extremities of the skeleton, which is uncommon.

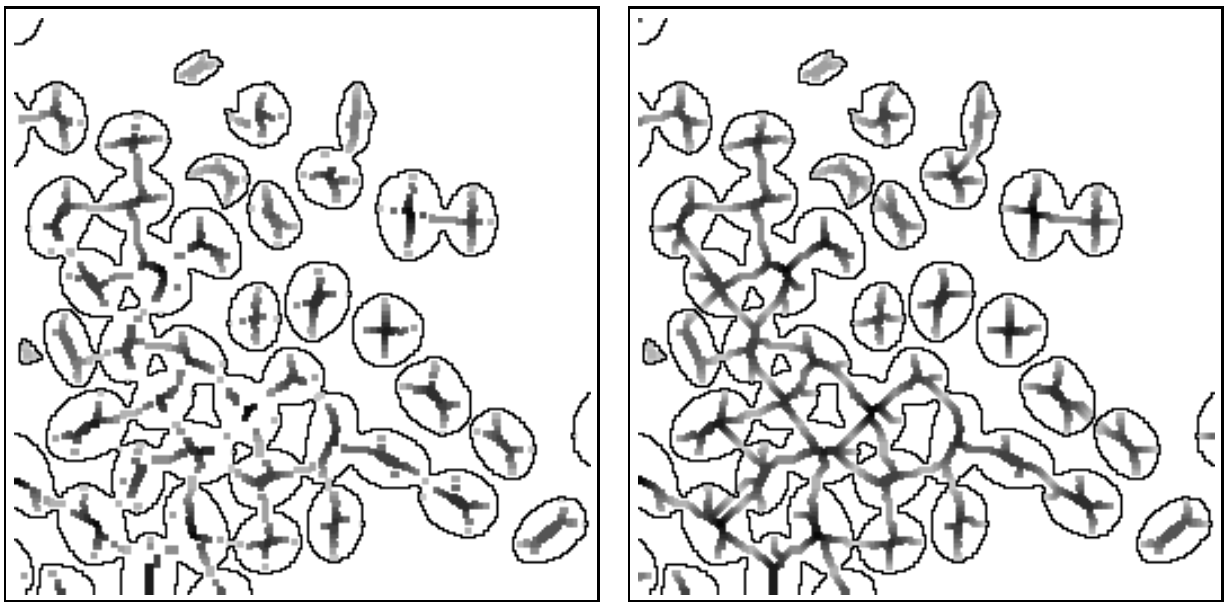

(a) *(b)*

Figure 21: *Quench function (a) and connected quench function (b). Their supports have been dilated for clarity.*

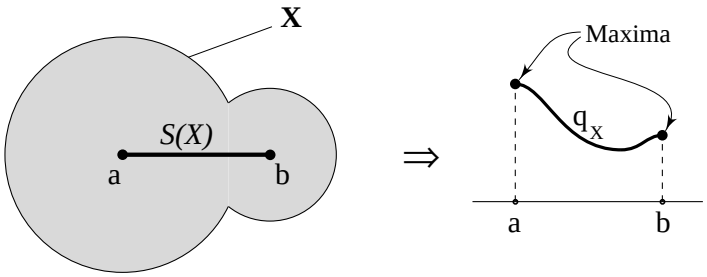

Figure 22: *Skeleton of a set X, associated quench function q_X and its maxima.*

Definition 13 (Local maximum) *A pixel p of a grayscale image I is a local maximum if and only if for every pixel q which is neighbor of p, $I(p) \geq I(q)$.*

Obviously, if M is a regional maximum of I, then

$$p \in M \implies p \text{ is a local maximum,}$$

but the converse is does not hold, as we shall point out shortly. Similarly, one can define local and regional minima.

The problem with definition 11 is that the discrete quench function is defined on a non-connected support, so that its maxima are not really defined! To get around this problem, we can compute the maxima of the connected quench function presented earlier (see Fig. 21b). The thus extracted ultimate erosion of the coffee-beans image is shown in Fig. 23a.

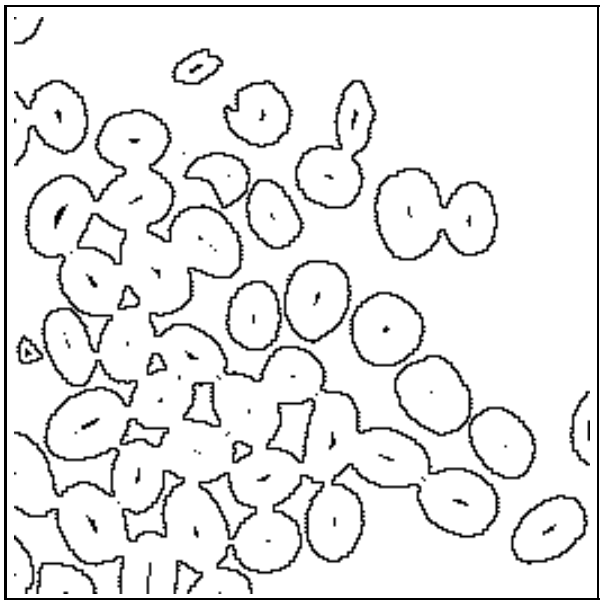

Figure 23: Ultimate erosion of the coffee beans image.

We can see that this ultimate erosion provides a reasonably good marking of our beans. We are therefore close to reaching our first goal, namely the extraction of one (connected) marker per object. There remain two points to address:

- the marking is still not perfect: some beans are multiply marked. How to reconnect some markers in order to end up with one single marker per bean?
- How to extract ultimate erosions in a more straightforward manner?

These two issues are addressed in the next section with the introduction of the distance function.

3.2.3 Ultimate Erosion and Distance Function

In this section, we give a completely different interpretation of the utimate erosion. Let X be a set made of overlapping components. When performing iterative erosions of this set with respect to the unit size ball B, its components are progressively shrunk and *separated* from the rest of the set before they are completely removed by the erosion process. This is illustrated by Fig. 24.

If, throughout this erosion process, we keep aside each connected component just before it is removed, it can be proved that the thus obtained set is exactly the ultimate erosion of X. Given two sets A and B such that $B \subseteq A$, let us denote by $\rho_A(B)$ the union of the connected components of A that have a non-empty

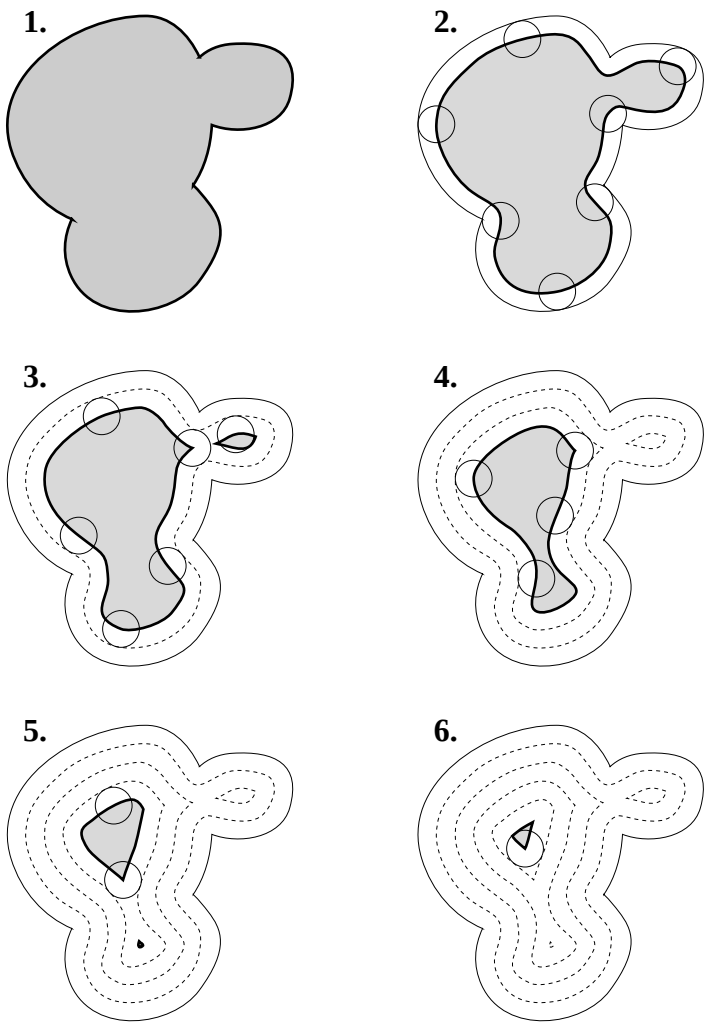

Figure 24: *Successive erosions of a set. Each component is separated from the rest of the set before it is removed by the erosion process.*

intersection with B. This operator is called *reconstruction* and is more fully discussed in section 3.3. Our new ultimate erosion algorithm can now be expressed by the following formula:

$$Ult(X) = \bigcup_{n \in \mathbb{N}} [(X \ominus nB) \setminus \rho_{X \ominus nB}(X \ominus (n+1)B)] \tag{22}$$

The resulting ultimate erosion of the set of Fig. 24 is shown inFig. 25.

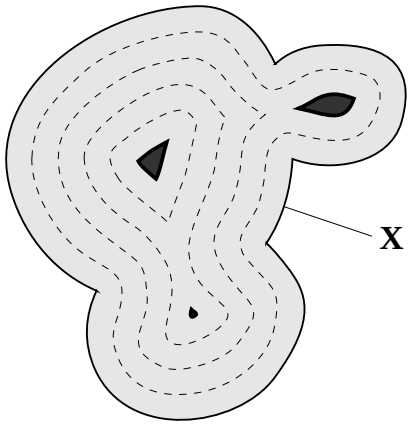

Figure 25: *Ultimate erosion of a set.*

This method suggests yet another way to determine the ultimate erosion of a X. Indeed, there is a morphological transformation which synthesizes all the information contained in the successive erosions of a set X. This transformation is called the *distance function* and associates with each pixel p of X the size of the first erosion of X that does not contain p:

Definition 14 (Distance function) *The distance function $dist_X$ associated with a set X is given by:*

$$\forall p \in X, \quad dist_X(p) = \min\{n \in \mathbb{N} \mid p \notin X \ominus nB\}. \tag{23}$$

For each pixel $p \in X$, $dist_X(p)$ is the distance between p and the background, i.e., X^C. The 8-connected distance funtion of the coffee beans image is shown in Fig. 26.

By definition, the regional maxima at altitude h of the distance function are the connected components at altitude h of $dist_X$ such that every neighboring pixel is of altitude strictly smaller than h. Any of these regional maxima are removed by a unit-size erosion. Indeed, if this was not true, there would exist pixels q located inside the regional maximum and verifying $dist_X(q) > h$, which is absurd. These maxima thus belong to the ultimate erosion of X and the following proposition can be derived:

Proposition 15 *The ultimate erosion of a set X is equal to the union of the regional maxima of the distance function of X.*

Since distance functions and regional maxima can be computed very efficiently in discrete images (see e.g. [54]), this last proposition provides the best computational method for extracting ultimate erosions. As a matter of curiosity, what happens if we now extract the *local* maxima of the distance function? The following proposition holds:

Proposition 16 *The skeleton by maximal balls of a set X is equal to the set of local maxima of its distance function.*

The distance function is therefore at the basis of a very large number of morphological algorithms. Later in this chapter, it will be used conjunction with the watershed algorithm. For completeness of this section, we shall also mention that after local and regional maxima, the *crest-lines* of the distance function are of

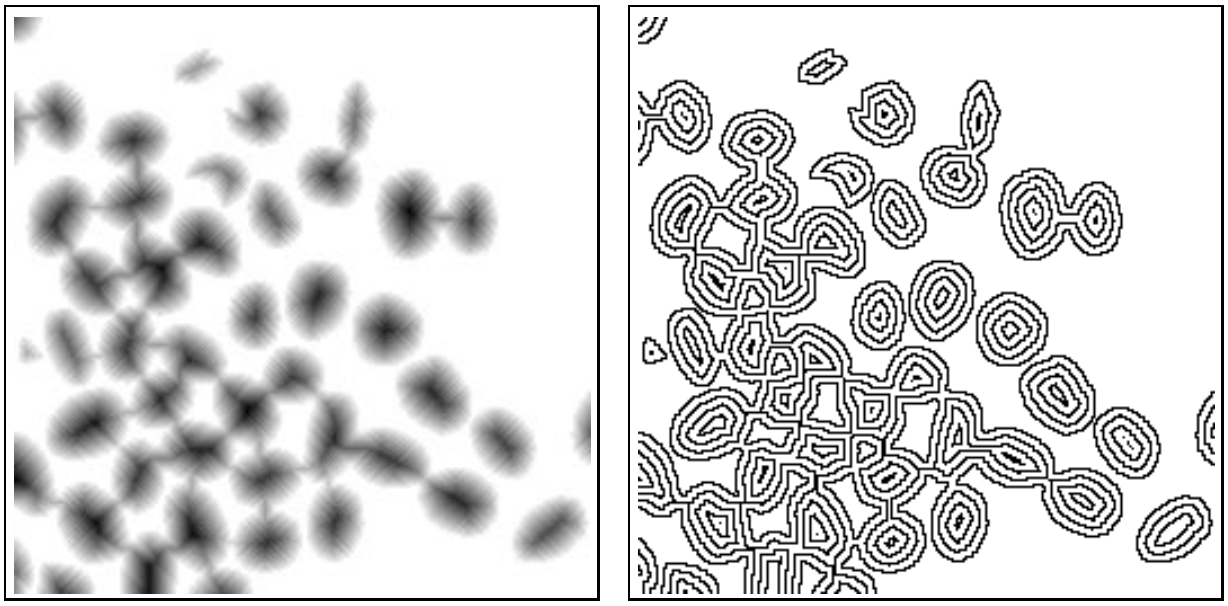

(a) *(b)*

Figure 26: *8-connected distance function of the coffee beans image (a) and level lines of this function (b).*

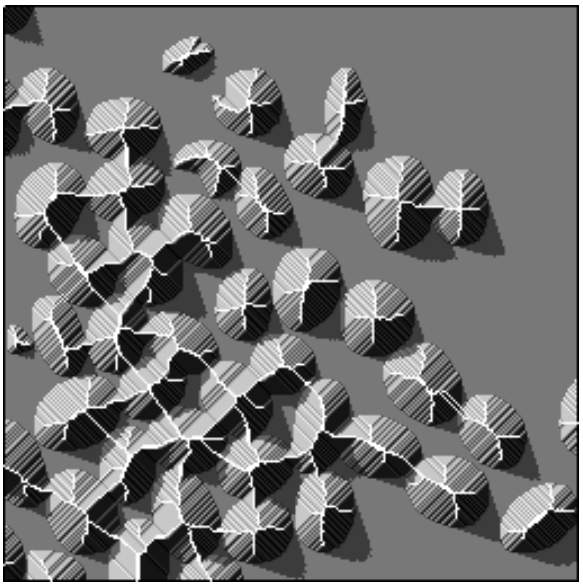

Figure 27: *The skeleton follows the crest-lines of the distance function.*

interest: following them allows us to extract the connected skeleton of X (see Fig. 27). This forms the basis of a series of algorithms proposed by F. Meyer [46, chapter 13].

We have now defined the morphological tools that will allow us to obtain perfect bean markers. We saw on Fig. 23 that the ultimate erosion does not quite yield perfect markers of our beans: all beans are marked, but some have multiple markers. The disconnections are caused by our dicrete workspace as well as small contour irregularities of the beans. For this particular image, a unit size dilation would be good enough to-reconnect the markers and end up with one single marker per bean. However, this might not work in the general case: components of the ultimate erosion marking the same coffee bean may indeed be separated by arbitrarily large distances.

The method used instead relies upon the fact that two components of the ultimate erosion marking the same bean are pretty much on the same "maximal zone" of the distance function. In fact, it is possible to go from one to the other on the distance function by going down no more than one level. Thus, if we subtract 1 from the distance function at the location of all the components of the ultimate erosion, we obtain a modified distance function whose maxima are exactly the desired bean markers, as illustrated in Fig. 28.

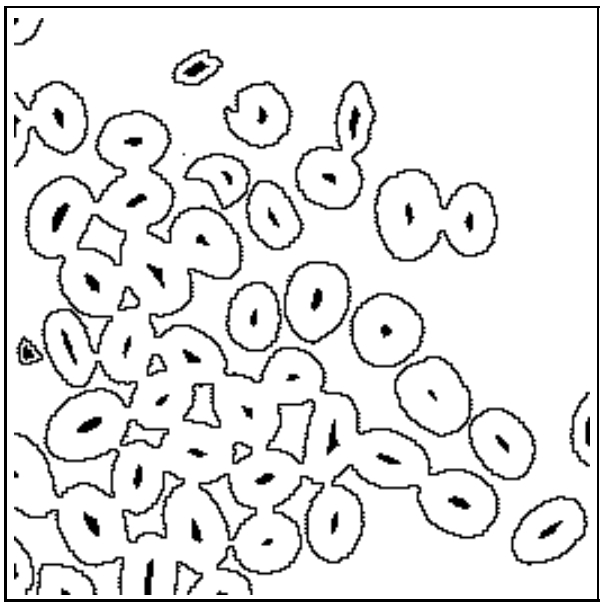

Figure 28: *Final bean markers. For this image as well as for Fig. 23, the exact Euclidean distance function was used.*

3.2.4 Skeleton by Influence Zones

The last concept that we need to define in this section is that of *skeleton by influence zones,* also called *SKIZ.*

Definition 17 *Let X be a set made of n connected components $(X_i)_{1\leq i\leq n}$. The influence zone $Z(X_i)$ of X_i is the locus of the points which are closer to it than to any other connected component of X:*

$$Z(X_i) = \{p \in \mathbb{Z}^2 \mid \forall j \neq i, d(p, X_i) \leq d(p, X_j)\}. \tag{24}$$

The distance d used in this equation is the discrete distance induced by the grid we are using (4-, 6-, or 8-connectivity),

The SKIZ is then defined as follows:

Definition 18 (SKIZ) *The SKIZ of set X, denoted SKIZ(X), is the set of the boundaries of the influence zones $\{Z(X_i)\}_{1\leq i\leq n}$.*

An example of skeleton by influence zones is shown on Fig. 29a. Just as the skeleton follows the crest-lines of the distance function, one can view the SKIZ as folowing the valley-lines of the inverted distance function of the background (Fig. 29b).

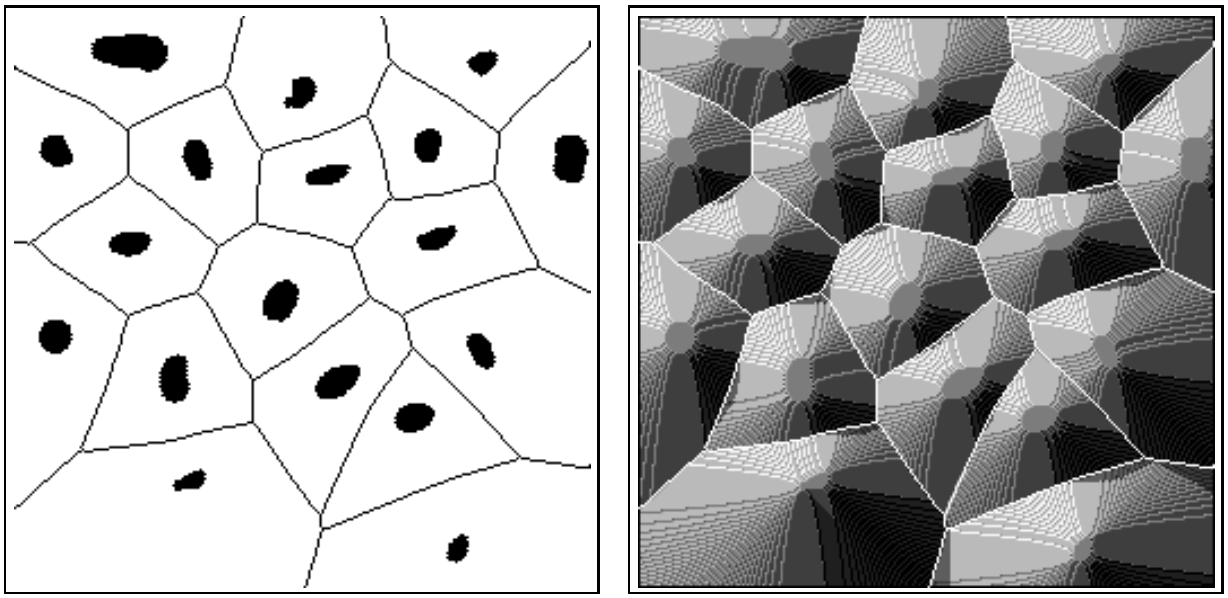

(a) *(b)*

Figure 29: SKIZ of a binary image; (b) the SKIZ follows the valley lines of the inverted distance function of the background. This example was computed using Euclidean distance.

3.3 Geodesic Transformations

3.3.1 Introduction, Geodesic Distances

At this point, we have achieved the first step of our segmentation as outlined in section 3.1: the marker extraction. It now remains to make good use of these markers for the extraction of correct set boundaries. The idea is to define each bean as the image region centered around its marker. Our intent is therefore to "grow" these markers back in the mask of the coffee-beans image. For this purpose, we now need the notion of *geodesic* operators introduced by C. Lantuéjoul [29, 30].

Contrary to classic "Euclidean" morphological operations, geodesic ones do not operate on the entire space, but on a finite set X which is called the *mask*. They are based on the notion of geodesic distance:

Definition 19 *The geodesic distance between two points x and y of X is the infimum of the length of the paths between x and y in X, if such paths exist:*

$$d_X(x,y) = \inf\{l(C_{x,y}) \mid C_{x,y} \text{ is a path between } x \text{ and } y \text{ included in } X\}. \tag{25}$$

If there are no such paths, we set $d_X(x,y) = +\infty$.

This definition is illustrated by Fig. 30

We call the *geodesic ball* of radius n and of center $p \in X$ the set $B_X(p,n)$ defined by:

$$B_X(p,n) = \{p' \in X, d_X(p',p) \leq n\}. \tag{26}$$

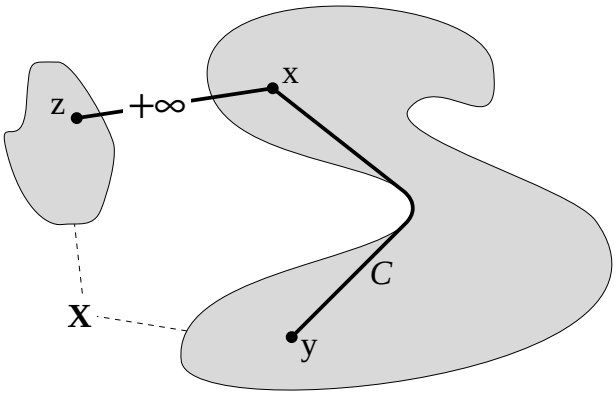

Figure 30: *Geodesic distance in a set X.*

3.3.2 Geodesic Dilations and Erosions

Suppose now that X is equipped with its associated geodesic distance d_X. Given $n \geq 0$, we consider the *structuring function* [46] mapping each pixel $p \in X$ to the geodesic ball $B_X(p, n)$ of radius n centered at p. This leads to the definition of the *geodesic dilation* of a subset Y of X:

Definition 20 *The geodesic dilation $\delta_X^{(n)}(Y)$ of size n of set Y inside set X is given by*

$$\delta_X^{(n)}(Y) = \bigcup_{p \in Y} B_X(p, n) = \{p' \in X, \exists p \in Y, d_X(p', p) \leq n\}. \tag{27}$$

The dual formulation of the geodesic erosion of size n of Y inside X is the following:

$$\varepsilon_X^{(n)}(Y) = \{p \in Y \mid B_X(p, n) \subseteq Y\} = \{p \in Y \mid \forall p' \in X/Y, d_X(p, p') > n\}. \tag{28}$$

Examples of geodesic dilation and erosion are shown in Fig. 31.

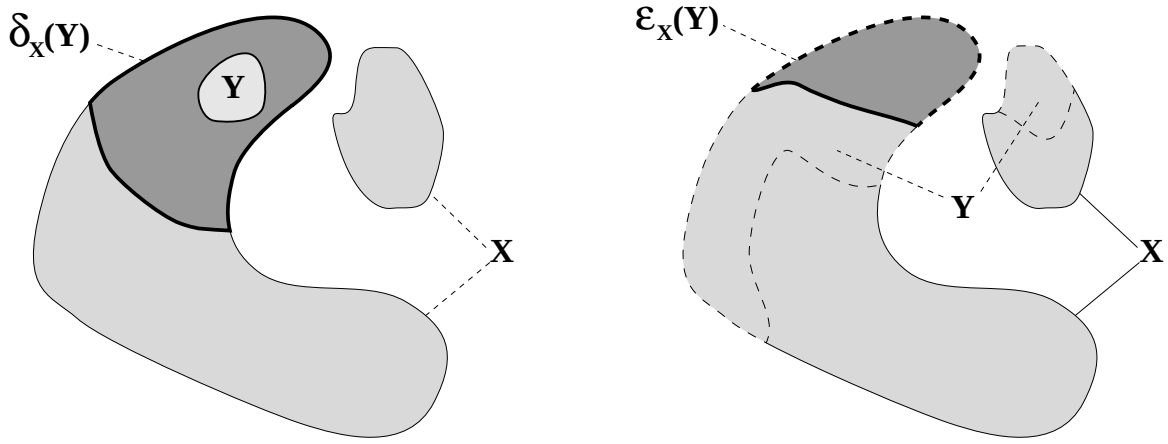

Figure 31: *Examples of a geodesic dilation and of a geodesic erosion of set Y inside set X.*

As already mentioned, the result of a geodesic operation on a set $Y \subseteq X$ is always included in X, which is our new workspace. As far as implementation is concerned, an elementary geodesic dilation (of size 1) of

a set Y inside X is obtained by intersecting the result of a unit-size dilation of Y (with respect to the unit ball B) with the workspace X:

$$\delta_X^{(1)}(Y) = (Y \oplus B) \cap X. \tag{29}$$

A geodesic dilation of size n is obtained by iterating n elementary geodesic dilations:

$$\delta_X^{(n)}(Y) = \underbrace{\delta_X^{(1)}(\delta_X^{(1)}(\ldots\delta_X^{(1)}}_{n \text{ times}}(Y))). \tag{30}$$

One can derive similar equations for geodesic erosions.

3.3.3 Reconstruction and Applications

One can notice that by performing successive geodesic dilations of a set Y inside a set X, it is impossible to intersect a connected component of X which did not initially contain a connected component of Y. Moreover, in this successive geodesic dilation process, we progressively "reconstruct" the connected components of X that were initially *marked* by Y. This is shown in Fig. 32.

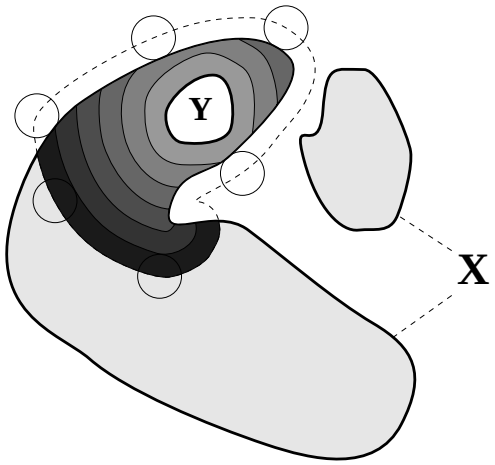

Figure 32: Successive geodesic dilations of set Y inside set X.

Now, the sets with which we are concerned are finite ones. Therefore, there exists n_0 such that

$$\forall n > n_0, \quad \delta_X^{(n)}(Y) = \delta_X^{(n_0)}(Y).$$

At step n_0, we have entirely reconstructed all the connected components of X which were initially marked by Y. This operation is naturally called *reconstruction:*

Definition 21 (Reconstruction) *The reconstruction $\rho_X(Y)$ of the (finite) set X from set $Y \subseteq X$ is given by the following formula:*

$$\rho_X(Y) = \lim_{n \to +\infty} \delta_X^{(n)}(Y). \tag{31}$$

Fig. 33 illustrates this transformation.

Some applications require that the various markers remain unconnected (this is the case, for instance, of the binary segmentation problem with which we are concerned). In such cases, the *geodesic influence zones* of the connected components of set Y inside X are used. Indeed, the notions of influence zones and of SKIZ presented in section 3.2.4 easily extend to the geodesic case, as shown by Fig. 34.

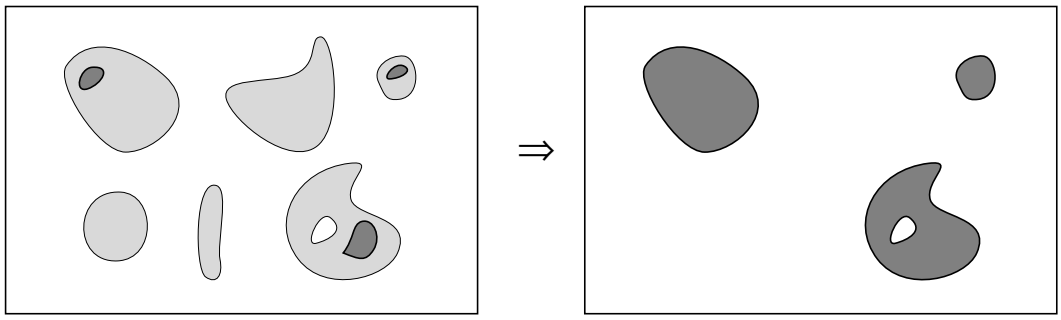

Figure 33: Reconstruction of X (light set) from Y (dark set).

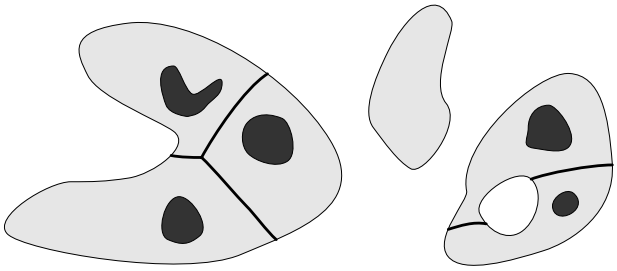

Figure 34: Example of geodesic SKIZ.

3.3.4 Grayscale Reconstruction

At present, all the tools required for solving our bean segmentation problem have been defined. However for grayscale segmentation, we will also need to extend the concept of geodesy to grayscale images.

It has been known for several years that—at least in the discrete case—any increasing transformation defined for binary images can be extended to grayscale images [45, 60, 47]. By increasing, we mean a transformation ψ such that

$$\forall X, Y \subset \mathbb{Z}^2, \quad Y \subseteq X \Longrightarrow \psi(Y) \subseteq \psi(X). \tag{32}$$

In order to extend such a transformation ψ to grayscale images I taking their values in $\{0, 1, \ldots, N\}$, it suffices to consider the successive thresholds $T_k(I)$ of I, for $k = 0$ to N:

$$T_k(I) = \{p \in D_I \mid I(p) \geq k\}, \tag{33}$$

where D_I is the domain of image I. They are said to constitute the *threshold decomposition* of I [33]. As illustrated by Fig. 35, these sets obviously satisfy the following inclusion relationship:

$$\forall k \in [1, N], \quad T_k(I) \subseteq T_{k-1}(I).$$

When applying the increasing operation ψ to each of these sets, their inclusion relationships are preserved. Thus, we can now extend ψ to grayscale images as follows:

$$\forall p \in D_I, \quad \psi(I)(p) = \max\{k \in [0, N] \mid p \in \psi(T_k(I))\}. \tag{34}$$

In the present case, binary geodesic reconstruction is an increasing transformation in that it satisfies:

$$Y_1 \subseteq\ Y_2, X_1 \subseteq X_2, \quad Y_1 \subseteq\ X_1, Y_2 \subseteq\ X_2 \quad \Longrightarrow \quad \rho_{X_1}(Y_1) \subseteq \rho_{X_2}(Y_2). \tag{35}$$

Therefore, following the threshold superposition principle of equation (34), we define grayscale reconstruction as follows [56]:

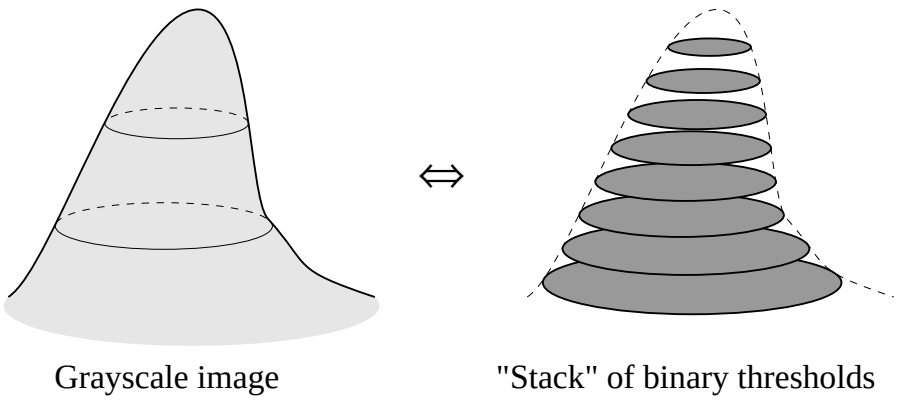

Figure 35: Threshold decomposition of a grayscale image.

Definition 22 (Grayscale reconstruction) *Let J and I be two grayscale images defined on the same domain, taking their values in the discrete set $\{0, 1, \ldots, N\}$ and such that $J \leq I$ (i.e., for each pixel $p \in D_I, J(p) \leq I(p)$). The grayscale reconstruction $\rho_I(J)$ of I from J is given by:*

$$\forall p \in D_I, \quad \rho_I(J)(p) = \max\{k \in [0, N] \mid p \in \rho_{T_k(I)}(T_k(J))\}.$$

Fig. 36 illustrates this transformation. Just like binary reconstruction extracts those connected components of the mask which are marked, grayscale reconstruction extracts the *peaks* of the mask which are marked by the marker-image.

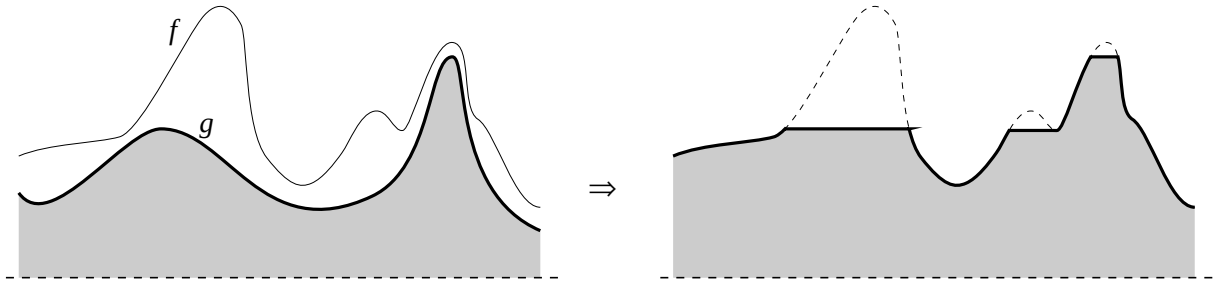

Figure 36: Grayscale reconstruction of mask f from marker g.

By duality, we are also able to define the *dual grayscale reconstruction,* or reconstruction by erosion:

Definition 23 (Dual grayscale reconstruction) *Let J and I be two grayscale images defined on the same domain, taking their values in the discrete set $\{0, 1, \ldots, N\}$ and such that $J \geq I$ (i.e., for each pixel $p \in D_I, J(p) \geq I(p)$). The grayscale reconstruction $\rho^*_I(J)$ of I from J is given by:*

$$\forall p \in D_I, \quad \rho_I(J)(p) = N - \rho_{N-I}(I - J).$$

3.3.5 Binary Segmentation

Let us now use all these tools to design a powerful binary segmentation algorithm. Starting from the markers of our objects, i.e. from the ultimate erosion, our goal is to accurately outline these objects. We could consider using the geodesic SKIZ, and defining each object as the geodesic influence zone of its marker inside the initial set. Unfortunately, this is not a satisfactory algorithm. Indeed, as shown in Fig. 37, the separating lines thus defined between objects are poorly located. This is due to the fact that the *altitudes* of the different markers—i.e. the value associated with them by the quench function—is not accounted for by this method.

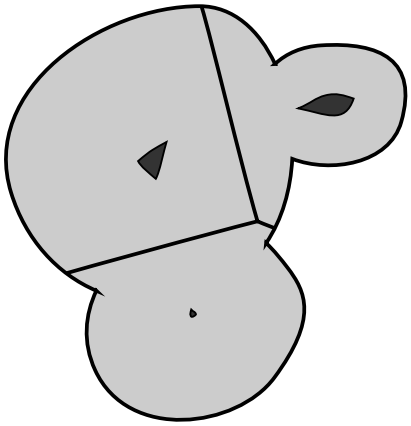

Figure 37: *Bad segmentation algorithm: geodesic SKIZ of the ultimate erosion of X inside X.*

The way to design a good segmentation procedure—in taking the above altitudes into account—is to use the geodesic SKIZ repeatedly. Let n_m be the size of the largest nonempty erosion of X:

$$X \ominus n_m B \neq \emptyset \quad \text{and} \quad X \ominus (n_m + 1)B = \emptyset.$$

$X \ominus n_m B$ is obviously a subset of the ultimate erosion of X. Denote this set by X_{n_m}. Now, consider the erosion of size $n_m - 1$ of X, i.e. $X \ominus (n_m - 1)B$. Obviously, the following inclusion relation holds:

$$X_{n_m} \subseteq X \ominus (n_m - 1)B.$$

Now, let Y be a connected component of $X \ominus (n_m - 1)B$. There are three possible inclusion relations between Y and $Y \cap X_{n_m}$:

1. $Y \cap X_{n_m} = \emptyset$: in this case, Y is another connected component of $Ult(X)$.
2. $Y \cap X_{n_m} \neq \emptyset$ and is connected: here, Y is used as a new marker.
3. $Y \cap X_{n_m} \neq \emptyset$ and is not connected: in this last case, the new markers are the geodesic influence zones of $Y \cap X_{n_m}$ inside Y.

These three different cases are shown on Fig. 38.

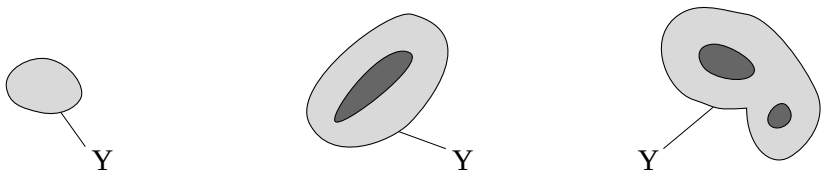

Figure 38: *The three possible inclusion relations between Y and $Y \cap X_{n_m}$.*

Let $X_{n_m - 1}$ be the set of markers produced after this step. To summarize what we have just said, $X_{n_m - 1}$ is made of the union of:

- the geodesic influence zones of X_{n_m} inside $X \ominus (n_m - 1)B$,
- the connected components of $Ult(X)$ whose *altitude* is $n_m - 1$.

This procedure is then iterated at levels $n_m - 2$, $n_m - 3$, etc... until level 0 is reached. In a more formal way, for every $0 < n < n_m$, let us introduce the following notations:

(i) $u_n(X)$ is the set of connected components of $Ult(X)$ having altitude n:

$$p \in u_n(X) \quad \Longleftrightarrow \quad p \in Ult(X) \text{ and } dist_X(p) = n.$$

(ii) For every set $Y \subseteq X$, $z_X(Y)$ designates the set of geodesic influence zones of the connected components of Y inside X.

The recursion formula between levels n and $n-1$ can now be stated:

$$X_{n-1} = z_{X \ominus (n-1)B}(X_n) \cup u_{n-1}(X). \tag{36}$$

It is illustrated by Fig. 39.

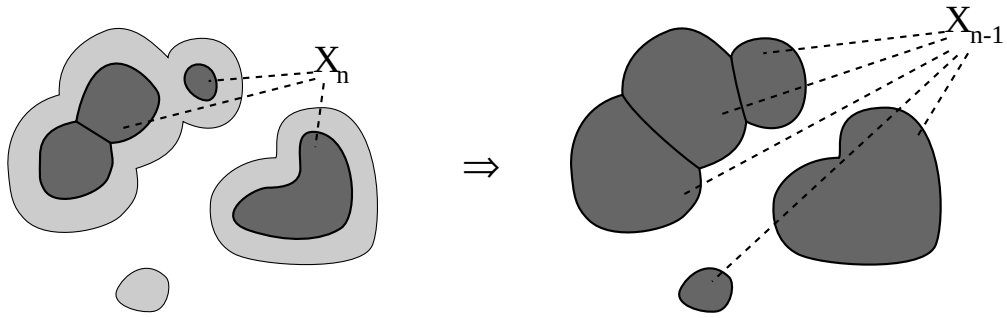

Figure 39: How to obtain X_{n-1} from X_n.

The set X_0 that is finally obtained after applying this algorithm constitutes a correct segmentation of X. Fig. 40 presents an example of this binary segmentation algorithm. Applying these notions to the bean segmentation problem, we see in Fig. 41 that, whereas a geodesic SKIZ of our markers results in improper separating lines, the segmentation algorithm we just described yields an accurate segmentation of the beans.

3.4 Watersheds and Grayscale Segmentation

3.4.1 Deriving a General Segmentation Approach

As presented in section 3.3.5, our morphological binary segmentation algorithm is rather complicated. In the present section, we give a much more intuitive approach to it. Consider the function (grayscale image) $-dist_X$, where $dist_X$ is the distance function introduced in section 3.2.3, and regard it as a topographic surface. The *minima* of this topographic surface are located at the different connected components of the ultimate erosion of X. Now, if a drop of water falls at a point p of $-dist_X$, it will slide along the topographic surface, following some steepest slope path, until it finally reaches one of its minima. We define the *catchment basin* $C(m)$ associated with a minimum m of our topographic surface in the following way:

Definition 24 (Catchment basin) *The catchment basin $C(m)$ associated with a (regional) minimum m of a grayscale image regarded as a topographic surface is the locus of the points p such that a drop falling at p slides along the surface until it reaches m.*

This definition is not very formal, but has the advantage of being intuitive. In our example, the catchment basins of the function $-dist_X$ exactly correspond to the regions that were extracted by the algorithm presented in section 3.3.5, as illustrated by Fig. 42. The segmentation achieved in section 3.3.5 exactly corresponds to extracting the catchment basins of the opposite of the distance function.

In fact, the notion of catchment basin can be defined for any kind of grayscale image. Moreover, the algorithm of section 3.3.5 can be easily adapted to the determination of the basins of any grayscale image

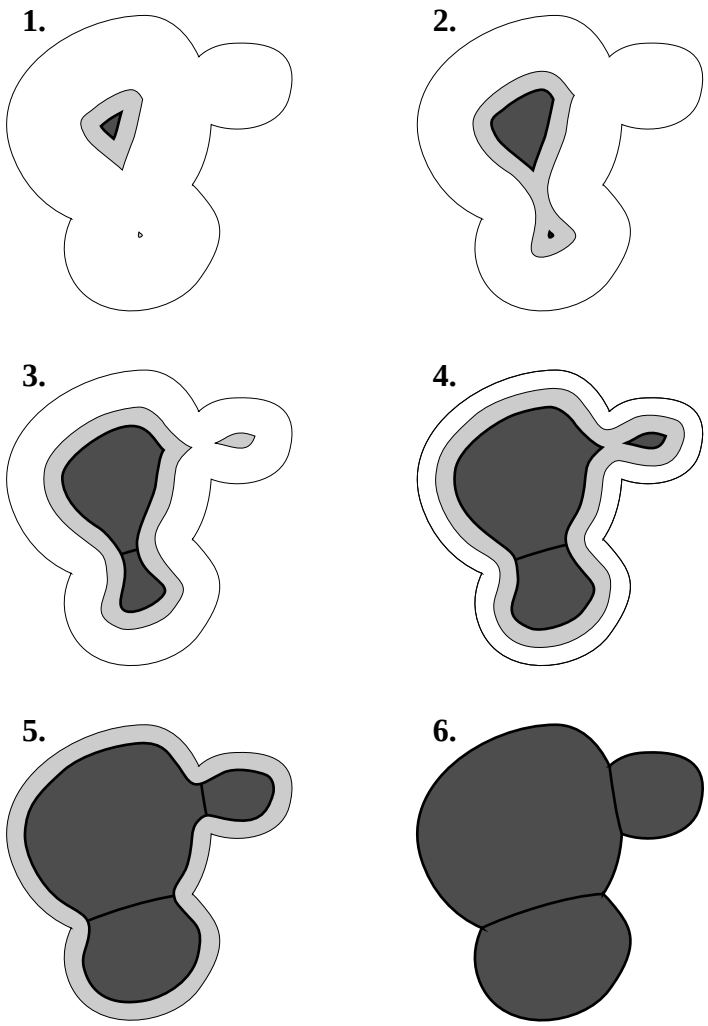

Figure 40: Correct binary segmentation algorithm presented in section 3.3.5.

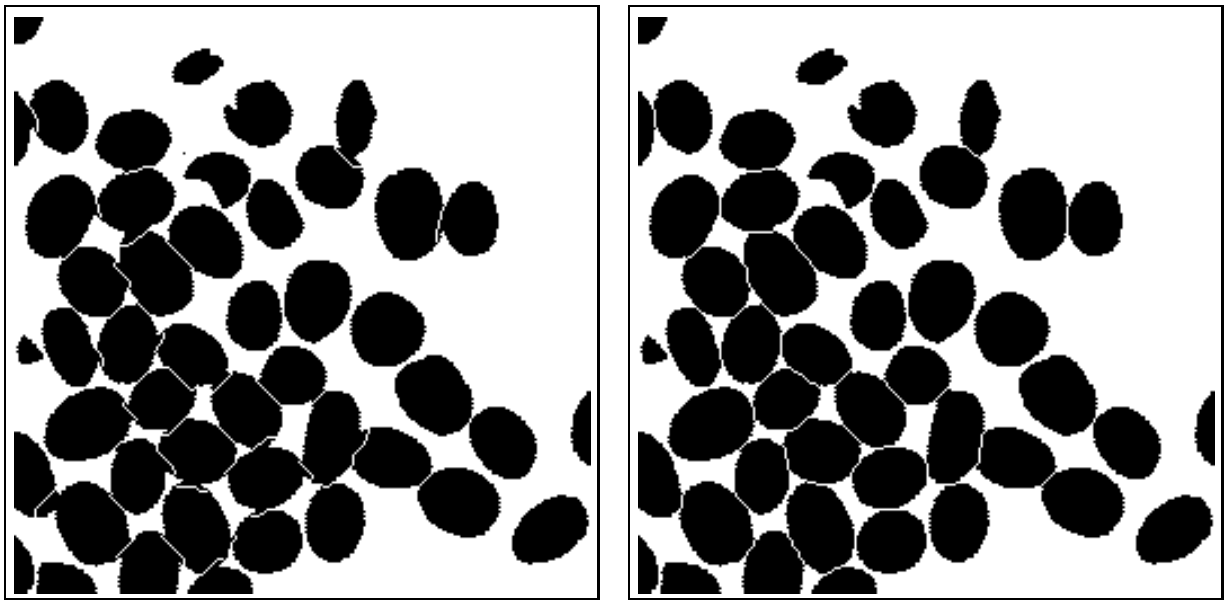

(a) geodesic SKIZ *(b) correct segmentation*

Figure 41: Segmentation of coffee beans from their markers.

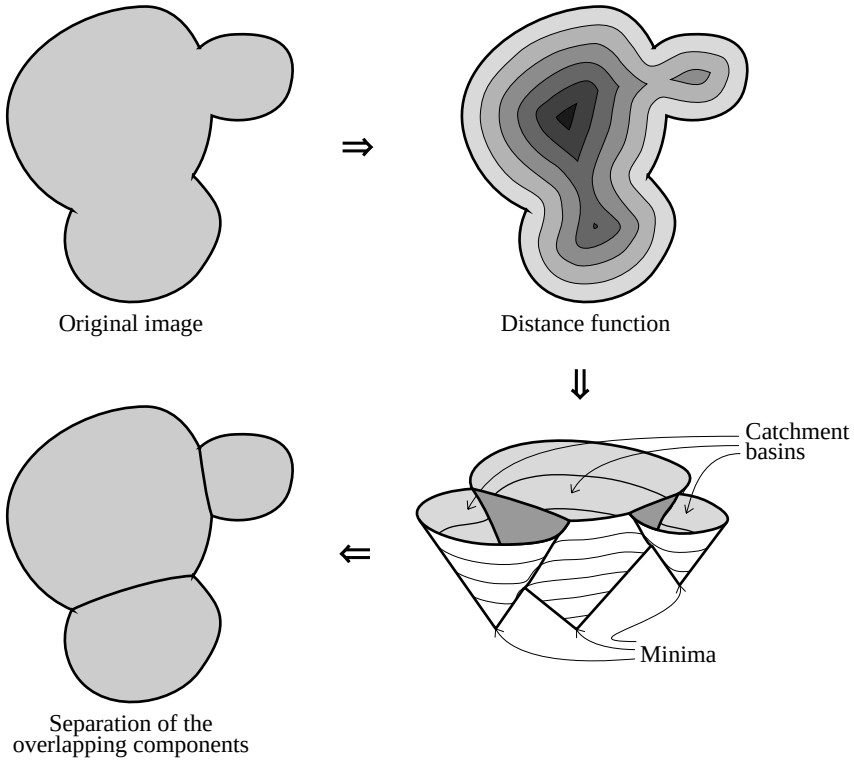

Figure 42: Interpretation of binary segmentation in terms of catchment basins of the opposite of the distance function.

I: it suffices to replace the successive erosions $X \ominus nB$—which correspond to the different thresholds of the distance function of X—by the successive thresholds of I (for more details, refer to [59]). The crest-lines separating different basins are called *watersheds lines* or simply *watersheds.*

Definition 25 (Watersheds) *The watersheds (lines) of a grayscale image I are the lines that separate the different catchment basins of I.*

These notions are illustrated by Fig. 43.

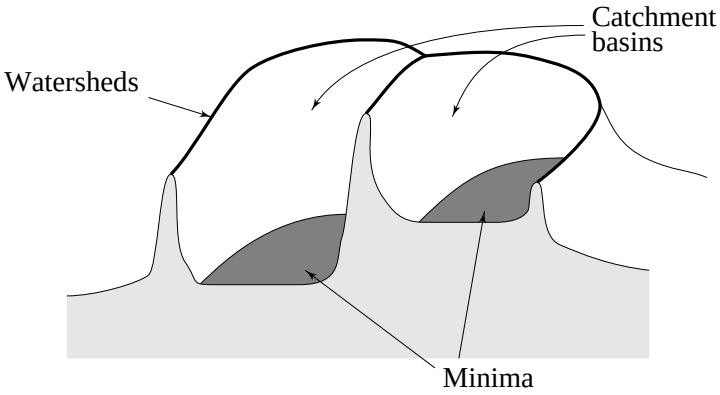

Figure 43: *Regional minima, catchment basins, and watershed lines.*

Watersheds stand out as a powerful morphological crest-line extractor. It is therefore most interesting to apply the watershed transformation to gradient images: indeed, the contours of a grayscale image can be viewed as the regions where the gray levels exhibit the fastest variations, i.e., the regions of maximal gradient. These regions are the *crest-lines of the gradient.* This remark is illustrated by Fig. 44 and is at the basis of the use of watersheds for grayscale segmentation, as described and illustrated in [6, 4, 57, 59].

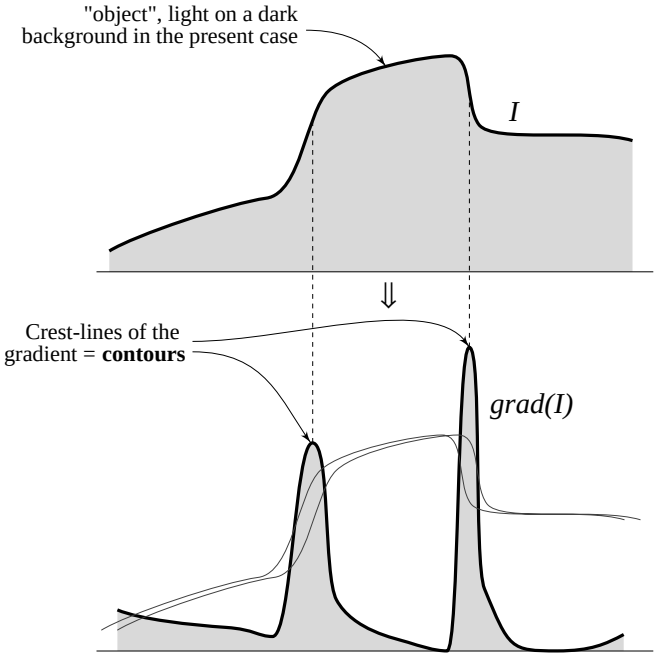

Figure 44: *Principle of grayscale segmentation via watersheds of the gradient.*

Note that in morphology, the word *gradient* refers to an operation associating with each image pixel the *modulus* of its gradient—in the classical sense of the word. Most of the time, the gradient known as *Beucher's gradient* [45] is used, which is obtained as the algebraic difference of a unit-size dilation and a unit-size erosion of I:

$$grad(I) = (I \oplus B) - (I \ominus B).$$

Nonetheless, depending on the type of image contours to be extracted, other gradients may be of interest: directional gradients, asymmetric gradients, regularized gradients, etc [39].

The watershed transformation always provides *closed* contours and constitutes a very general approach to contour detection. However, it can very rarely be used directly on gradient images without resulting in dramatic *over-segmentations:* the image gets partitioned in far too many regions, i.e., the correct contours are lost in a large number of irrelevant ones! This problem is mainly due to noise in the data: noise in the original image results in noise in its morphological gradient, this in turn causing it to exhibit far too many regional minima. This directly translates into far too many catchment basins, i.e., over-segmentation!

Several approaches have been proposed in literature to overcome this over-segmentation: for example, some techniques remove arcs of the watersheds based on an integration of the gradient's gray values along them. Others take the dual point of view and merge adjacent regions (i.e., catchment basins here) when the gray level of the original image over them is comparable. None of these techniques is satisfactory in that it is very difficult to incorporate to them knowledge specific to the collection of images under study. Besides, they go against the point of view presented at the beginning of this section, claiming that marker extraction should be the first step of every segmentation.

Therefore, the morphological approach to this problem consists in making use of image-specific knowledge (e.g., size, shape, location or brightness of the objects to extract) to design robust object marking procedures [57, 59, 7]. This step of the segmentation can be completely different from one problem to another. Not only must each object be uniquely marked, the *background* also needs its own marker(s). In a second step, this binary image of markers is used, not to guide region-merging or arc-removal algorithms, but on the contrary, to *modify the gradient image* on which watersheds are computed.

More precisely, let I denote the original grayscale image, $J = grad(I)$ its morphological gradient, and let M denote the binary image of markers. The "modification" of J should result in a grayscale image J' with the following characteristics:

- its only regional minima are exactly located on the connected components of M (M is the set of "imposed" minima);
- its only crest-lines are the highest crest-lines of J that are located between the imposed minima.

The watersheds of J' are thus the highest crest-lines of $grad(I)$ that separate our markers. Hence, they are the *optimal contours* corresponding to set of markers M and gradient J.

The actual computation from J and M of an image J' with these characteristics has been classically achieved using a three-step process [57]:

1. Set to $h_{\min}$ any pixel of J that is located on a marker, $h_{\min}$ being chosen such that $\forall p, h_{\min} < J(p)$. This results in a new image J^*:

$$\forall p, \quad J^*(p) = \begin{cases} h_{\min} & \text{if } M(p) = 1 \\ J(p) & \text{otherwise.} \end{cases}$$

2. Create the following grayscale image M^*

$$\forall p, \quad M^*(p) = \begin{cases} h_{\min} & \text{if } M(p) = 1 \\ h_{\max} & \text{otherwise,} \end{cases}$$

   where $h_{\max}$ is chosen such that $\forall p, J(p) < h_{\max}$.

3. Use M^* to remove all the unwanted minima of J^* while preserving its highest crest-lines between markers. This is done using the dual grayscale reconstruction operation ρ^*:

$$\forall p, \quad J'(p) = \rho^*_{J^*}(M^*). \tag{37}$$

This process is illustrated by Fig. 45. The watersheds of the resulting image J' provide the desired segmentation.

The whole procedure presented above is often referred to as *marker-driven watershed segmentation.* It is extremely powerful in a number of complex segmentation cases, where it mostly reduces the segmentation task to (1) the choice of a gradient and (2) the extraction of object markers (this latter task can itself be very complex in some cases).

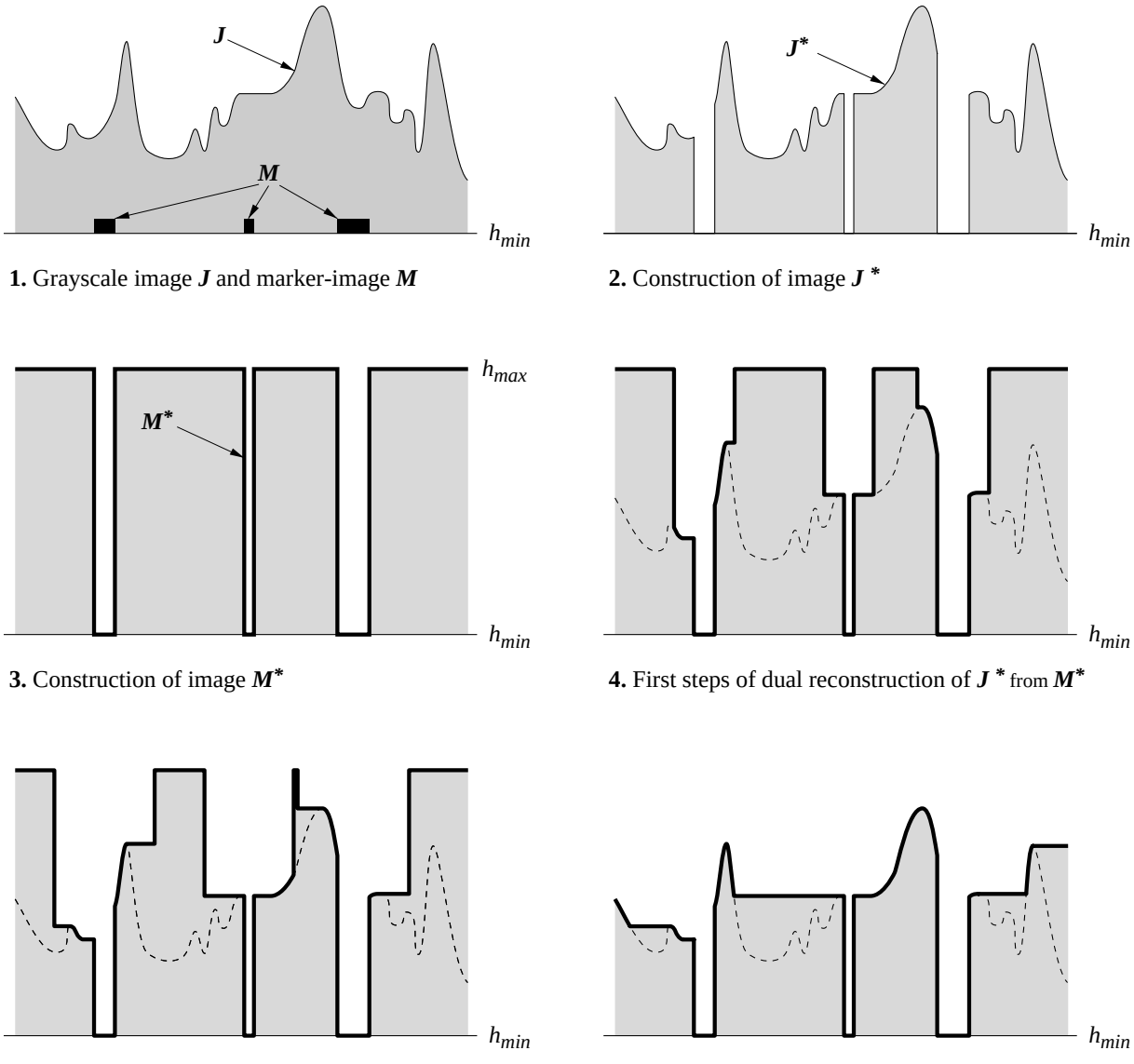

1. Grayscale image ***J*** and marker-image ***M***

2. Construction of image J^*

3. Construction of image M^*

4. First steps of dual reconstruction of J^* from M^*

5. Dual reconstruction of J^* from M^* (cont.)

6. Final modified image J'

Figure 45: *Use of dual grayscale reconstruction to "impose" a set M of minima to a grayscale image J.*

3.4.2 The Electrophoresis Example

Let us illustrate this segmentation paradigm on the two-dimensional electrophoresis image of Fig. 46a (see also [3, 57]). The standard morphological gradient of this image is shown in Fig. 46b. As mentioned above, if we simply compute the watersheds of Fig. 46b, the result is clearly disappointing (See Fig. 46c). Indeed,

the gradient exhibits a large number of minima, mainly due to the presence of noise in the original image. Nevertheless, one can notice that *all* the spots are marked by these minima and hence all the correct contours are present in Fig. 46c. The watershed simply produces *over-segmentation.*

Avoiding over-segmentation requires the prior extraction of correct spot markers. Since the spots constitute the dark part of the image, they should be interpreted as the image minima. Yet, the direct extraction of the initial image's minima is not a satisfactory solution, as illustrated by Fig. 46d: once again, many of these mimina are due to acquisition noise in our data. Here however, filtering image 46a (with a morphological filter called an *alternating sequential filter (ASF)*, see [46, chapter 10] or [47]) is sufficient to produce an image whose minima correctly mark the spots (See Figs. 46e-f).

In fact, this marker extraction step is followed by binary watershed segmentation in order to cut markers like the upper-right corner one, which clearly should mark two different spots. The final image of object markers is shown in Fig. 47a. As concerns the background marker, it is extracted as the set of the highest crest-lines of the original image that separate the spot markers. This is the best way to assure that it will be located on the lightest areas of the image and separate all the object markers. Its determination is done in a similar way as gradient modification (see Eq. 37 and Fig. 45). It is shown in Fig. 47b.

Both sets of markers are then combined in a final marker image, shown in Fig. 47c. It is used to modify the gradient of Fig. 46b, this resulting in Fig. 47d. The watersheds of the latter image provide the desired segmentation, as shown in Figs. 47e-f.

The result is in accordance with our expectations: each spot has a unique contour which is located on the inflexion points of the initial luminance function—i.e. the original image. Given the extracted set of markers, we found the optimal gradient crest-lines, i.e. the best possible segmentation for these markers and, to a lesser extent, this gradient.

3.4.3 Difficult Segmentations, Recent Developments

Hierarchical watershed segmentations The method described in the previous section can be applied to a wide range of problems, as long as the preliminary marker extraction step can be performed with sufficient accuracy. However, in some difficult segmentation cases, it is impossible to find markers of the regions or of the objects to extract, since these objects or regions are not themselves well defined. This kind of situation often occurs, for instance, with remote sensing images, where the large variety of zones (fields, roads, houses, towns, lakes, etc, under different lighting conditions) makes it almost impossible to design robust marking procedures.

In this latter case, region-growing types of techniques (see beginning of section 3.4.1) may provide an appropriate solution. In fact, a few morphological region-growing techniques based on the watershed transformation have recently been proposed and seem very promising:

- In the first one, "raw" watershed segmentation is applied to the gradient of the original image, thus resulting in an over-segmented image of catchment basins. Each catchment basin C is assigned a uniform gray-level corresponding, for example, to the mean gray-level of the pixels of the original image over C. In a second step, this "mosaic image" is regarded as a graph (the dual adjacency graph, see Fig. 48), and morphological operations are performed on this graph [50] in order to merge adjacent regions with comparable gray-levels. In fact, graph-gradients and graph-watersheds can themselves be iteratively applied to the original adjacency graph. This results in an image pyramid containing a hierarchy of contours at different resolutions [51].

- Starting again from an over-segmented "mosaic" of catchment basins (resembling Fig. 46c), some methods introduced by S. Beucher process the adjacency graph *of the watershed arcs.* Catchment basins are hierarchically merged via recursive removal of these contour elements in the graph [5].

- Lastly, in [41], Ph. Salembier and J. Serra approach the problem of general image segmentation via a combination of filters and watersheds that is started at coarse scales and progressively refined into more and more detailed segmentations. Their approach is therefore a region-splitting one, as opposed to the previous region-growing approaches.

Obviously, the watersheds are of enormous interest for complex segmentation problems, and the above solutions are barely starting to explore the extraordinary possibilities of this tool.

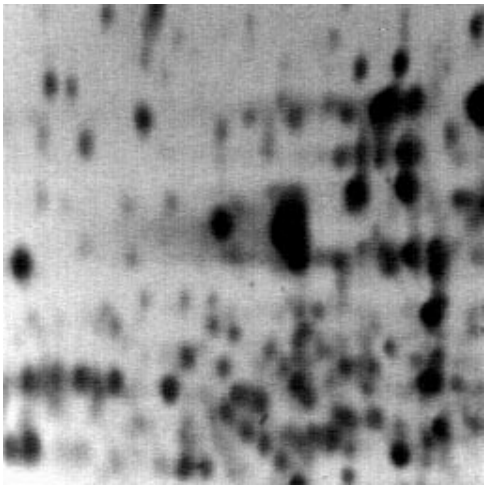

(a) original image

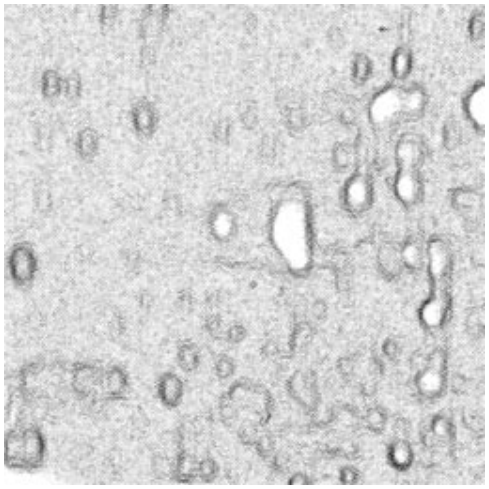

(b) gradient of original image

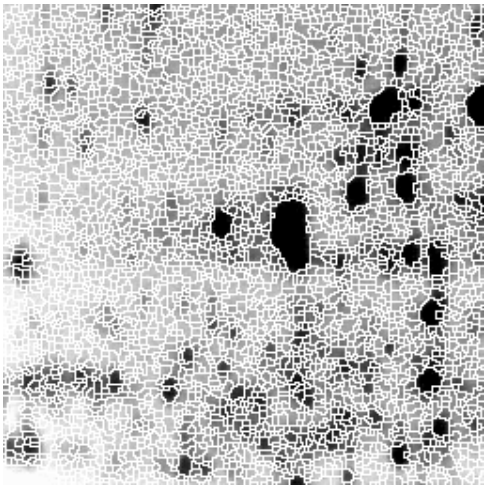

(c) watersheds of gradient

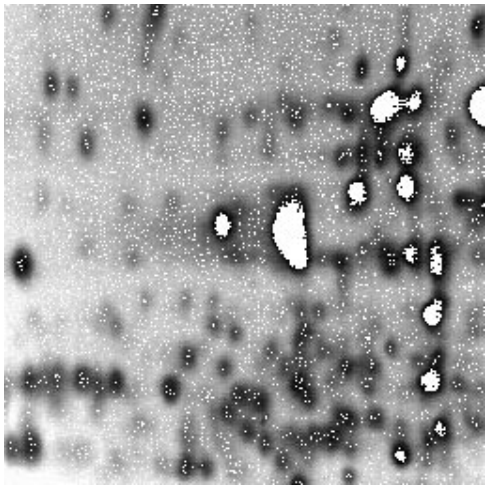

(d) minima of original image

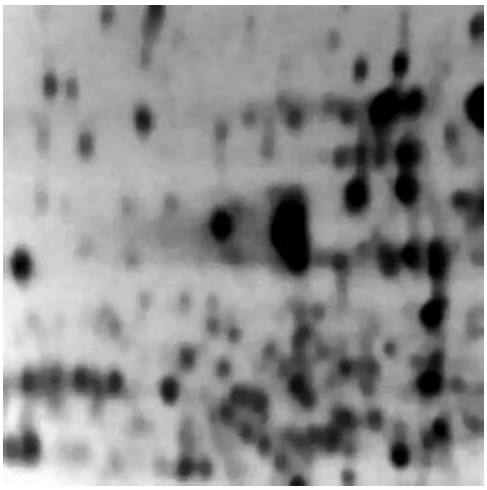

(e) AS-filtered image

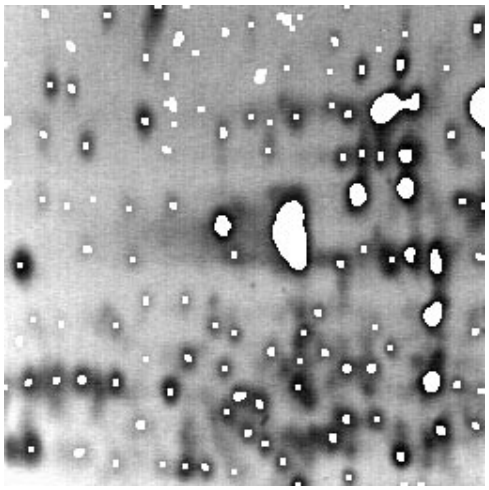

(f) minima of filtered image

Figure 46: Segmentation of electrophoresis gels (1)

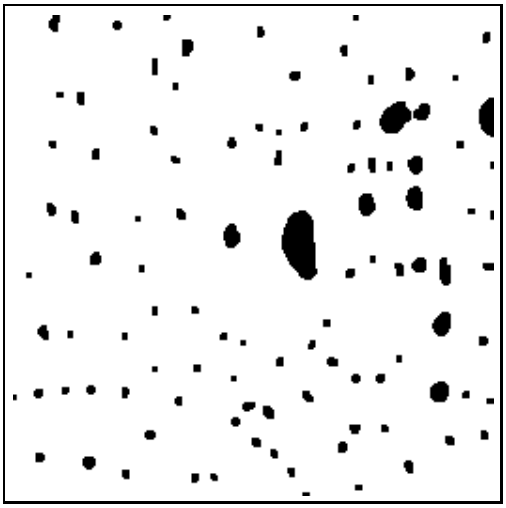

(a) final spot markers

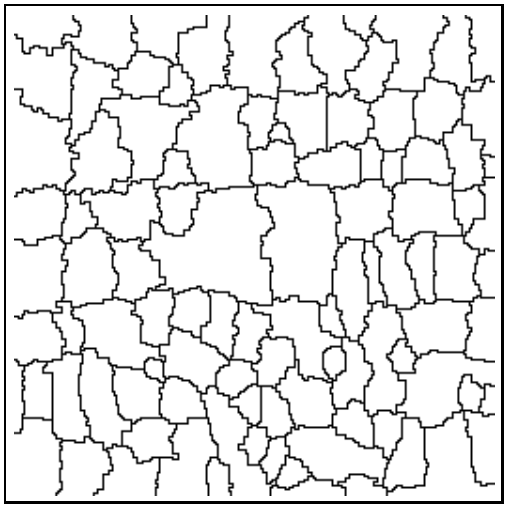

(b) background marker

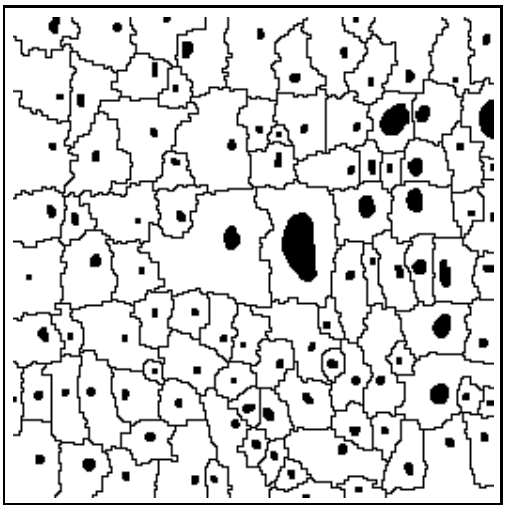

(c) complete set of markers

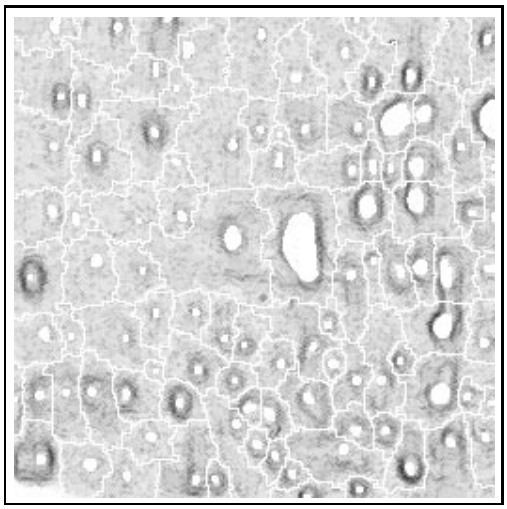

(d) modified gradient

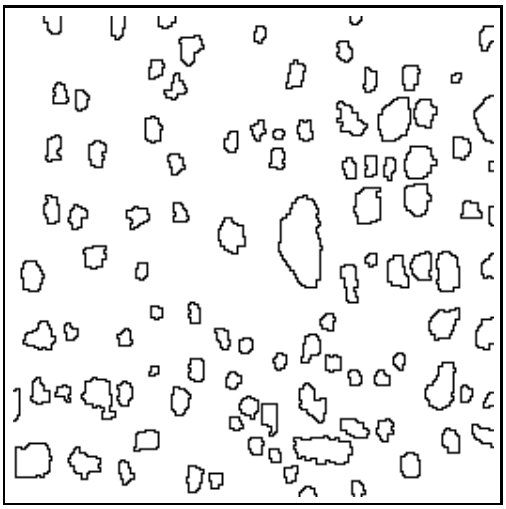

(e) watersheds of modified gradient

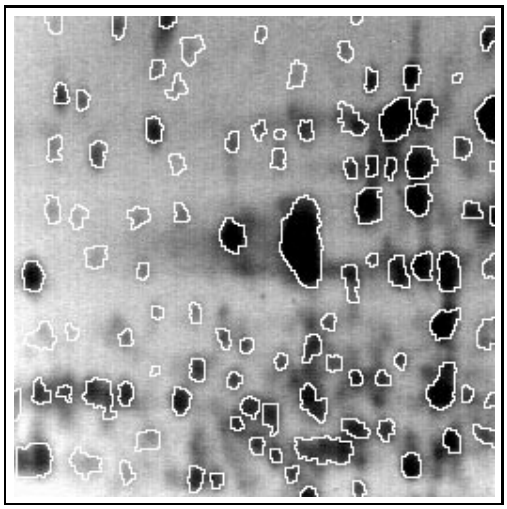

(f) overlayed result

Figure 47: Segmentation of electrophoresis spots (2)

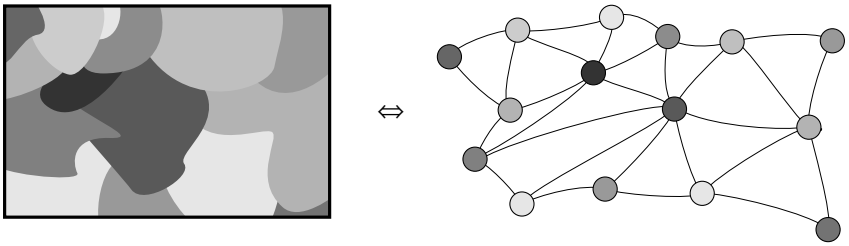

Figure 48: Mosaic image and associated adjacency graph.

Segmentation of Intricately Overlapping Particles In binary segmentation, the marking by ultimate erosion has its limitations [57]: it is only efficient if, on the one hand, the components of the set X under study are "sufficiently blobby", and on the other hand, if they do not overlap too much. For instance, when X is composed of two overlapping discs, they are both marked by ultimate erosion if and only if their centers are located on either sides of the radical axis (See Fig.49).

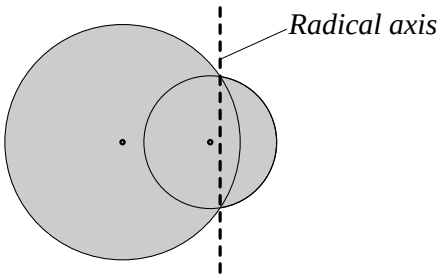

Figure 49: These two discs overlap too much to be both marked by ultimate erosion

However, there exist more sophisticated marking tools. Among them, let us mention a transformation called *conditional bisector* (see [37, page 55] or [49]), in which the marking is no longer related to the maxima of the quench function but to the extrema of its derivative. For $\theta \in [0, \pi/2]$, $X \in \mathbb{R}^2$, and assuming that the skeleton $S(X)$ is continuously differentiable, the θ-conditional bisector of X can be defined as follows:

Definition 26 *The θ-conditional bisector of X, denoted $CB_\theta(X)$ is the set of points of $S(X)$ where the derivative of the quench function q_X along the skeleton is within $[-\tan(\theta), \tan(\theta)]$.*

An efficient algorithm for computing discrete approximations of $CB_\theta(X)$ for any θ has been proposed in [49]. It is extremely useful for marking "sharp" portions of sets.

Similarly, when the set to be segmented is made up of elongated particles, it may be of interest to mark their extremities. This can be achieved either via techniques based on geodesic ultimate erosions or by means of the maxima of the *propagation function* [31, 44].

Let us illustrate how the conditional bisector can be used to solve a complex binary segmentation application. Fig. 50a is a binary image of a cross section of vitreous fibers. These fibers are overlapping and need to be separated. A very acceptable marking of these fibers was proposed in [48] (Fig. 50b), resulting in the first watershed segmentation shown in Fig. 50c. However, since some intricately overlapping fibers were not marked, they are not separated in Fig. 50c (these particles are pointed at by arrows).

In order ot mark them, a $\pi/6$-conditional bisector was used (see Fig. 50d). Not only does it mark these fibers, it also marks some "necks" between fibers. The latter are eliminated as crossing the separating lines of Fig. 50c (see Fig. 50e). Now, since some of the resulting markers are still slightly disconnected, a connection technique described in [25, 49] was used: Fig. 50e is dilated by a unit size disc, resulting in Fig. 50f. The latter

image is then skeletonized with the constraint that the pixels of Fig. 50e belong to the resulting skeleton (see [52] for more details on constrained skeletons). This results in Fig. 50g. Adding to this image the markers of Fig. 50b yields the final marker-image shown in Fig. 50h. At this stage, a new watershed segmentation provides the (almost) perfect result of Fig. 50i.

4 Conclusions

In this chapter we first dealt with the segmentation of images of textures. We showed that granulometries and their moments constitute a general approach to the segmentation and classification of such images. In order to keep the chapter simple, only the binary case was presented, but the methods extend to grayscale images, as illustrated by the example of Fig. 10. This section showed that adequate combinations of simple morphological operations (namely openings and closings in the present case) can lead to powerful segmentation algorithms.

This statement becomes even clearer in the case of object segmentation problems: we started from elementary operations and progressively constructed a set of more and more elaborate tools that finally lead to watersheds and grayscale reconstruction. As illustrated on numerous examples, they are extremely powerful operations for binary and grayscale object segmentation problems. In addition, throughout the second part of this chapter, we attempted to derive a general philosophy of object segmentation using mathematical morphology. The outcome of this can be summarized in just two words: *markers* and *watersheds.*

The examples presented have each illustrated a different aspect of this morphological approach to segmentation. However, in no way are these examples full-size applications! There is practically no trivial segmentation problem, and with each new problem, comes a load of new difficulties to overcome: this leads to new ways to combine existing operations, or even to completely new transformations. The above segmentation philosophy should only be considered as a guideline for the image analyst and should not put any constraints on his or her creativity. In this way, each new application will lead to new advances and the field of morphology will keep progressing and being continually enriched with new operations.

References

[1] B. Bettoli and E. Dougherty. Linear granulometric moments of noise-degraded images. In *EURASIP Workshop on Mathematical Morphology and its Applications to Signal Processing*, Barcelona, May 1993.

[2] B. Bettoli and E. Dougherty. Linear granulometric moments of noisy images. Technical Report MIL-02-93, Morphological Imaging Laboratory, Rochester Institute of Technology, Rochester, NY, Feb. 1993.

[3] S. Beucher. Analyse automatique des gels d'electrophorèse bi-dimensionnels et morphologie mathématique. Technical report, Ecole des Mines, CGMM, Paris, 1982.

[4] S. Beucher. Watersheds of functions and picture segmentation. In *IEEE Int. Conf. on Acoustics, Speech and Signal Processing*, pages 1928–1931, Paris, May 1982.

[5] S. Beucher. *Segmentation d'Images et Morphologie Mathématique.* PhD thesis, Ecole des Mines, Paris, June 1990.

[6] S. Beucher and C. Lantuéjoul. Use of watersheds in contour detection. In *International Workshop on Image Processing, Real-Time Edge and Motion Detection/Estimation*, Rennes, France, 1979.

[7] S. Beucher and F. Meyer. The morphological approach to segmentation: the watershed transformation. In E. R. Dougherty, editor, *Mathematical Morphology in Image Processing*, pages 433–481. Marcel-Dekker, Sept. 1992.

[8] C. Bhagvati, D. Grivas, and M. Skolnick. Morphological analysis of surface condition. In E. R. Dougherty, editor, *Mathematical Morphology in Image Processing*, pages 121–150. Marcel-Dekker, Sept. 1992.

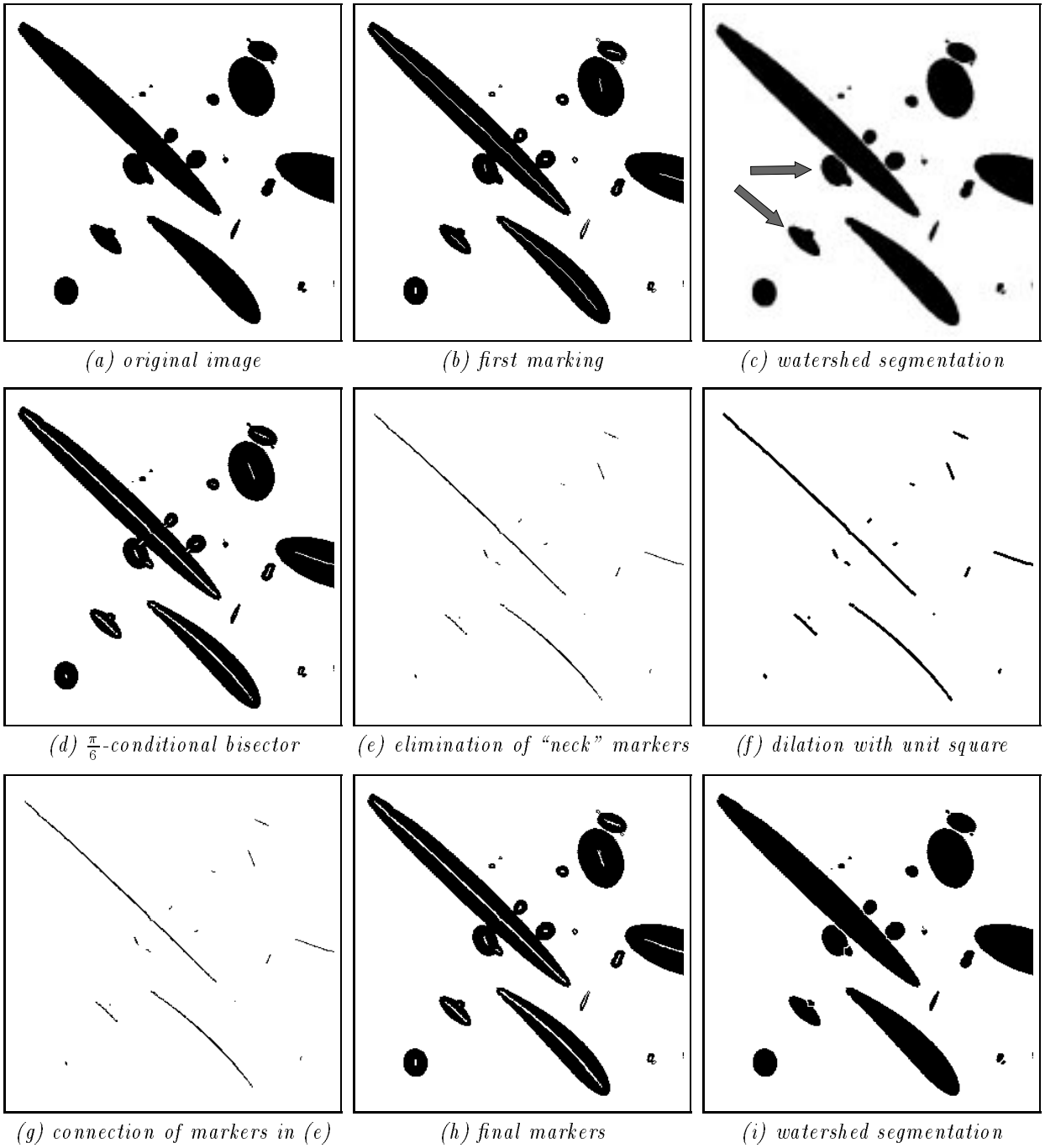

(a) original image *(b) first marking* *(c) watershed segmentation*

(d) $\frac{\pi}{6}$-conditional bisector *(e) elimination of "neck" markers* *(f) dilation with unit square*

(g) connection of markers in (e) *(h) final markers* *(i) watershed segmentation*

Figure 50: Use of conditional bisector and watersheds for the segmentation of binary images of glass fibers.

[9] H. Blum. An associative machine for dealing with the visual field and some of its biological implications. In E. Bernard and M. Kare, editors, *Biological Prototypes and Synthetic Systems*, pages 244–260. Plenum Press, New York, 1962. Proc. second Annual Bionics Symposium, Cornell University, 1961.

[10] G. Borgefors. Distance transformations in digital images. *Comp. Vis., Graphics and Image Processing*, 34:334–371, 1986.

[11] J. Brandt and V. Algazi. Lossy encoding of document images using the continuous skeleton. In *SPIE Vol. 1818, Visual Communications and Image Processing*, Boston MA, Nov. 1992.

[12] L. Calabi and W. Harnett. Shape recognition, prairie fires, convex deficiencies and skeletons. Technical Report 1, Parke Math. Lab. Inc., One River Road, Carlisle MA, 1966.

[13] Y. Chen and E. Dougherty. Texture classification by gray-scale morphological granulometries. In *SPIE Vol. 1818, Visual Communications and Image Processing*, Boston MA, Nov. 1992.

[14] Y. Chen and E. Dougherty. Gray-scale morphological granulometric texture classification. Technical Report MIL-16-92, Morphological Imaging Laboratory, Rochester Institute of Technology, Rochester, NY, Nov. 1993.

[15] Y. Chen, E. Dougherty, S. Totterman, and J. Hornak. Classification of trabecular structure in magnetic resonance images based on morphological granulometries. *Journal of Magnetic Resonance Medicine*, 1993. to appear.

[16] P. Danielsson. Euclidean distance mapping. *Comp. Graphics and Image Processing*, 14:227–248, 1980.

[17] E. Dougherty and G. C.R. *Image Processing: Continous to Discrete.* Prentice-Hall, Englewood Cliffs, NJ, Jan. 1987.

[18] E. Dougherty, J. Newell, and J. Pelz. Morphological texture-based maximum-likelihood pixel classification based on local granulometric moments. *Pattern Recognition*, 25(11), Nov. 1992.

[19] E. Dougherty and J. Pelz. Morphological granulometric analysis of electrophotographic images—size distribution statistics for process control. *Optical Engineering*, 30(4), Apr. 1991.

[20] E. Dougherty, J. Pelz, F. Sand, and A. Lent. Morphological image segmentation by local granulometric size distributions. *Journal of Electronic Imaging*, 1(1), Jan. 1992.

[21] E. R. Dougherty. Euclidean gray-scale granulometries: Representation and umbra inducement. *Journal of Mathematical Imaging and Vision*, 1(1), Mar. 1992.

[22] E. R. Dougherty. *An Introduction to Morphological Image Processing.* SPIE Press, Bellingham, WA, Feb. 1992.

[23] C. Giardina and E. Dougherty. *Morphological Methods in Image and Signal Processing.* Prentice-Hall, Englewood Cliffs NJ, 1988.

[24] M. Golay. Hexagonal pattern transforms. *IEEE Trans. on Computers*, 18(8), 1969.

[25] G. G. Gordon and L. Vincent. Application of morphology to feature extraction for face recognition. In *SPIE/SPSE Vol. 1658, Nonlinear Image Processing III*, pages 151–164, San Jose CA, Feb. 1992.

[26] M. Grimaud. A new measure of contrast: Dynamics. In *SPIE Vol. 1769, Image Algebra and Morphological Image Processing III*, pages 292–305, San Diego CA, July 1992.

[27] R. Haralick and L. Shapiro. Survey: Image segmentation techniques. *Comp. Vis., Graphics and Image Processing*, 29:100–132, 1985.

[28] C. Lantuéjoul. Issues of digital image processing. In R. M. Haralick and J.-C. Simon, editors, *Skeletonization in Quantitative Metallography.* Sijthoff and Noordhoff, Groningen, The Netherlands, 1980.

[29] C. Lantuéjoul and S. Beucher. On the use of the geodesic metric in image analysis. *Journal of Microscopy*, 121:39–49, Jan. 1981.

[30] C. Lantuéjoul and F. Maisonneuve. Geodesic methods in quantitative image analysis. *Pattern Recognition*, 17(2):177–187, 1984.

[31] F. Maisonneuve and M. Schmitt. An efficient algorithm to compute the hexagonal and dodecagonal propagation function. In *5th European Congress For Stereology*, pages 515–520, Freiburg im Breisgau FRG, Sept. 1989. Acta Stereologica. Vol. 8/2.

[32] P. Maragos. Pattern spectrum and multiscale shape representation. *IEEE Trans. Pattern Anal. Machine Intell.*, 11(7):701–716, July 1989.

[33] P. Maragos and R. Ziff. Threshold superposition in morphological image analysis. *IEEE Trans. Pattern Anal. Machine Intell.*, 12(5), May 1990.

[34] G. Matheron. *Random Sets and Integral Geometry*. John Wiley and Sons, New York, 1975.

[35] G. Matheron. Examples of topological properties of skeletons. In J. Serra, editor, *Image Analysis and Mathematical Morphology, Volume 2: Theoretical Advances*. Academic Press, London, 1988.

[36] F. Meyer. Contrast feature extraction. In J.-L. Chermant, editor, *Quantitative Analysis of Microstructures in Material Sciences, Biology and Medicine*, Stuttgart, FRG, 1978. Riederer Verlag. Special issue of Practical Metallography.

[37] F. Meyer. *Cytologie Quantitative et Morphologie Mathématique*. PhD thesis, Ecole des Mines, Paris, 1979.

[38] I. Pitas and A. Venetsanopoulos. Morphological shape representation. *IEEE Trans. Pattern Anal. Machine Intell.*, 11(7), July 1989.

[39] J.-F. Rivest, P. Soille, and S. Beucher. Morphological gradients. In *SPIE/SPSE Vol. 1658, Nonlinear Image Processing III*, pages 139–150, Feb. 1992.

[40] A. Rosenfeld and J. Pfaltz. Distance functions on digital pictures. *Pattern Recognition*, 1:33–61, 1968.

[41] P. Salembier and J. Serra. Morphological multiscale image segmentation. In *SPIE Vol. 1818, Visual Communications and Image Processing*, Boston, MA, Nov. 1992.

[42] F. Sand and E. R. Dougherty. Asymptotic normality of the morphological pattern-spectrum moments and orthogonal granulometric generators. *Journal of Visual Communication and Image Representation*, 3(2), June 1992.

[43] F. Sand and E. R. Dougherty. Statistics of the morphological pattern-spectrum moments for a random-grain model. *Journal of Mathematical Imaging and Vision*, 1(2), July 1992.

[44] M. Schmitt. Variations on a theme in binary mathematical morphology. *Journal of Visual Communication and Image Representation*, 2(3):244–258, Sept. 1991.

[45] J. Serra. *Image Analysis and Mathematical Morphology*. Academic Press, London, 1982.

[46] J. Serra, editor. *Image Analysis and Mathematical Morphology, Volume 2: Theoretical Advances*. Academic Press, London, 1988.

[47] J. Serra and L. Vincent. An overview of morphological filtering. *Circuits, Systems and Signal Processing*, 11(1):47–108, Jan. 1992.

[48] H. Talbot. Binary image segmentation using weighted skeletons. In *SPIE Vol. 1769, Image Algebra and Morphological Image Processing III*, pages 393–403, San Diego, CA, 1992.

[49] H. Talbot and L. Vincent. Euclidean skeletons and conditional bisectors. In *SPIE Vol. 1818, Visual Communications and Image Processing*, pages 862–876, Boston, MA, Nov. 1992.

[50] L. Vincent. Graphs and mathematical morphology. *Signal Processing*, 16:365–388, Apr. 1989.

[51] L. Vincent. Mathematical morphology for graphs applied to image description and segmentation. In *Electronic Imaging West 89*, pages Vol. 1, pp. 313–318, Pasadena, CA, 1989.

[52] L. Vincent. Efficient computation of various types of skeletons. In *SPIE Vol. 1445, Medical Imaging V*, pages 297–311, San Jose, CA, 1991.

[53] L. Vincent. Exact euclidean distance function by chain propagations. In *IEEE Int. Computer Vision and Pattern Recog. Conference*, pages 520–525, Maui, HI, June 1991.

[54] L. Vincent. Morphological algorithms. In E. R. Dougherty, editor, *Mathematical Morphology in Image Processing*, pages 255–288. Marcel-Dekker, Inc., New York, Sept. 1992.

[55] L. Vincent. Morphological area openings and closings for grayscale images. In *NATO Shape in Picture Workshop*, pages 197–208, Driebergen, The Netherlands, Sept. 1992.

[56] L. Vincent. Morphological grayscale reconstruction in image analysis: Applications and efficient algorithms. *IEEE Transactions on Image Processing*, 2:176–201, Apr. 1993.

[57] L. Vincent and S. Beucher. The morphological approach to segmentation: an introduction. Technical report, Ecole des Mines, CMM, Paris, 1989.

[58] L. Vincent and B. Masters. Morphological image processing and network analysis of corneal endothelial cell images. In *SPIE Vol. 1769, Image Algebra and Morphological Image Processing III*, pages 212–226, San Diego, CA, July 1992.

[59] L. Vincent and P. Soille. Watersheds in digital spaces: an efficient algorithm based on immersion simulations. *IEEE Trans. Pattern Anal. Machine Intell.*, 13(6):583–598, June 1991.

[60] P. Wendt, E. Coyle, and N. Gallagher. Stack filters. *IEEE Transactions on Acoustics Speech and Signal Processing*, 34(4):898–911, Aug. 1986.